System-bath correlation function probed by conventional and time-gated stimulated photon echo

Boeij, Wim P. de; Pshenichnikov, Maxim S.; Wiersma, Douwe A.

Published in:
Journal of Physical Chemistry

DOI:
10.1021/jp961039m

Publication date:
1996

ARTICLES

System−Bath Correlation Function Probed by Conventional and Time-Gated Stimulated Photon Echo

Wim P. de Boeij, Maxim S. Pshenichnikov, and Douwe A. Wiersma*

Ultrafast Laser and Spectroscopy Laboratory, Department of Chemistry, Materials Science Centre, University of Groningen, Nijenborgh 4, 9747 AG Groningen, The Netherlands

Received: April 5, 1996; In Final Form: May 29, 1996[⊗]

We show how in the framework of the multimode Brownian oscillator model the system−bath correlation function can be derived from conventional and time-gated stimulated photon echo experiments and consideration of the linear optical spectra. Experiments are performed on the infrared dye DTTCI in room temperature solutions of ethylene glycol, methanol, and acetonitrile. The obtained correlation function is the sum of several Brownian oscillators, of which four are attributed to *intrachromophore* vibrational dynamics and the other three to solute−solvent dynamics. The ultrafast part of the correlation function on the time scale of the excitation pulses is interpreted as a free induction decay-like effect due to impulsive excitation of spectrally broad underlying vibrational structure in the dye's electronic transition. The slower parts are assigned to multiple time scale solute−solvent dynamics. The effect of vibrational coherences on the echo measurements is also analyzed; this analysis permits the dissection of the correlation function into a part due to intrachromophore dynamics and a part due to solvation dynamics. The spectral densities associated with these latter oscillators are located in the far infrared, in the same spectral region as probed by the optical Kerr effect. The measurements, however, provide no definite answer to the question of whether these spectral densities are the same.

1. Introduction

Most chemical reactions take place in a liquid state environment. It is therefore not surprising that physical chemists have a vested interest in the exploration of liquid state dynamics.[1−7] Since molecular motions in liquids occur on time scales from tens of femtoseconds upward, it was not until ultrafast lasers became available that time-resolved studies of liquids and solutions became an important option.[8−56] In the last decade many nonlinear optical effects have been explored in studies of solvent and solvation dynamics, and it was shown that each technique projects onto certain types of molecular motion. For instance, while the optical Kerr effect probes solvent motions associated with anisotropic Raman polarizabilities,[8−18] far-infrared spectroscopy only senses dipolar molecular motions,[57−59] while optical absorption and emission spectroscopies cover all molecular motions that couple to the optical transition.

Molecular dynamics in solution can be studied both in the time and frequency domain. In the time domain, optical Kerr effect,[8−18] pump−probe,[19−21] photon echo,[22−41] transient grating scattering,[42] time-gated fluorescence,[43−51] and transient absorption spectroscopy[52−56] are popular techniques to investigate solvent and solvation dynamics. In the frequency domain, resonance light scattering,[60,61] two-color picosecond CARS,[62,63] and absorption/emission spectroscopy[64] are probes of solvent dynamics as well. Often these techniques are complementary in terms of their sensitivity with respect to certain time scales, and it is therefore essential to explore both domains in order to acquire a complete picture of solvent motion. While Fourier-transform relations exist both for linear and nonlinear optical susceptibilities,[65−68] time-domain optical experiments have the possibility of creating a time-window through which molecular motion can be explored.[69] Time-domain measurements are also most suited to compare with molecular dynamics (MD) simulations,[70−80] which usually cover only the first tens of picoseconds of liquid state dynamics.

In addition to impressive progress in femtosecond laser technology, which made femtosecond optical studies of solvent dynamics possible, the last decade has also seen important theoretical developments that were crucial to a successful description of optical dynamics in liquids.[67,69−90] We refer here to the use of the multimode Brownian oscillator (MBO) model or spin-boson Hamiltonian to a phenomenological description of molecular motions in liquids.[67,81−90] While purely phenomenological, the MBO model has been extremely important to our conceptual grasp of many nonlinear optical effects as well as to our understanding of the relation between certain, seemingly unconnected, spectroscopic observables. For instance, Mukamel and co-workers showed that in the MBO model a direct link exists between optical dynamics as probed in photon echo and the Stokes shift dynamics as measured in a time-gated fluorescence experiment.[67] Both probe the solvent reorganization energy, a quantity that plays such a crucial role in electron-transfer reactions.[47]

In the MBO model a central role is played by the correlation function $M(t)$, which is defined as the correlation function of the fluctuations of the normalized transition-energy gap, $\omega(t)$: [83]

$$M(t) = \frac{\langle \Delta\omega(0)\, \Delta\omega(t) \rangle}{\langle \Delta\omega^2 \rangle} \tag{1}$$

(Strictly speaking, in the fully quantum-mechanical MBO model

[⊗] Abstract published in *Advance ACS Abstracts,* July 15, 1996.

S0022-3654(96)01039-8 CCC: $12.00

there are two *different* correlation functions, which, under certain conditions, become undistinguishable. This issue is addressed in section 2.1.) To a good approximation, $M(t)$ mimics the solvation correlation function extracted directly from a time-resolved fluorescence experiment. Once $M(t)$ is known, all linear and nonlinear spectroscopical observables can readily be calculated.[67]

Femtosecond photon echo has been used extensively to characterize solution dynamics.[22−41] These studies were pioneered by the Shank group, who showed that optical dephasing in solution occurs on multiple time scales and that its theoretical description calls for a formalism beyond the standard Bloch model.[22] Especially the failure of the Bloch and stochastic modulation (Kubo) model to capture the Stokes shift in emission inspired use of the MBO model. Since then, many femtosecond photon echo experiments have been simulated successfully using this theory.[22−26,28−33,37−41] Early on, the importance of intrachromophore vibrational dynamics on the echo decay was also recognized.[22] It was appreciated that in order to extract the solute−solvent dynamics, the effect of vibrations needed to be taken into account explicitly.[19−21,91−93] The beauty of the MBO model is that it can easily accommodate vibrational dynamics in the correlation function.[67]

While classic stimulated photon echo spectroscopies have brought out important aspects of $M(t)$, they failed to generate a system−bath correlation function capable of simulating both the linear optical spectra as well as the results of a variety of nonlinear optical experiments. The main reason for this failure is that in regular photon echo spectroscopies there is no direct relation between the echo decay and $M(t)$. This state-of-affairs also left the question unanswered whether or not there existed *at all* a system−bath correlation function that would fit all optical data or, to pose it differently, whether the spin-boson Hamiltonian is a good approximation for a description of solvent dynamics. The answer to this question is also directly relevant to theoretical work done on electron transfer in condensed phases.[47]

Recently it was established that a first-order estimate of $M(t)$ can rather easily be obtained from stimulated photon echo-maximum (peak) shift experiments.[94,95] This type of experiment was pioneered by the Ippen group in stimulated photon echo studies of condensed phase systems.[96,97] They demonstrated that in the Bloch model the echo-peak shift is directly related to the ratio of homogeneous versus inhomogeneous broadening in the system. Joo and Albrecht used echo-peak shift measurements to characterize spectral diffusion in solution, employing a stochastic model to interpret the data.[29] The Fleming group also sought to employ the echo-peak shift as probe for the inertial effect in solvation dynamics.[36] Recently the same group used echo-peak shift experiments to study dynamics in bacterial light-harvesting complexes at room temperature.[98] We pointed out that for early times photon echo-peak shift measurements exhibit some pitfalls and that the direct assignment of early time dynamics to solvation dynamics is questionable.[37]

In an echo-peak shift experiment the maximum of the echo signal is measured at a fixed waiting time between the second and third pulse (t_{23}) while scanning the delay between the first two excitation pulses (t_{12}). The shift of the echo maximum with respect to zero constitutes the observable, denoted from here on as echo-peak shift. The echo-peak shift as a function of t_{23} is referred to as the echo-peak shift function. It was recently shown by us that for a bimodal $M(t)$ the echo-peak shift function reflects fairly well the correlation function except for the initial fast part.[95] The reason for the breakdown of the similarity between $M(t)$ and the echo-peak shift function at short times was also examined. It was also pointed out that echo-peak shift measurements alone are not enough to detail $M(t)$ and that other echo experiments, in particular phase-locked pump−probe[99] and time-gated echo,[40,41] are needed to construct a complete picture of $M(t)$.

In this paper we demonstrate how, starting from the echo-peak shift function, we can obtain an optimal system−bath correlation function in the framework of the MBO model. We discuss also *time-gated* stimulated photon echo experiments and show that it is superior to conventional photon echo, as it provides the opportunity to characterize both the ultrafast and slow parts of $M(t)$. We show that finite pulse duration calculations are essential to extract $M(t)$ from these and other echo experiments. For solutions of the dye DTTCI in ethylene glycol, methanol, and acetonitrile we are successful in obtaining an $M(t)$ that describes all linear and nonlinear optical experiments. Given the approximations made in the MBO model, this is a remarkable feat and justifies the use of the MBO model toward a description of optical dynamics in condensed phase molecular systems. The spectral densities associated with the Brownian oscillators assigned to solute−solvent dynamics are shown to be located in the far-infrared spectral region and match quite well the low-frequency part associated with optical Kerr experiments. However, no definite conclusion can be drawn concerning the question of whether these spectral densities are the same as those exposed in optical Kerr effect measurements. We also conclude that non-Markovian dynamics is the proper terminology for a multiple time scale correlation function as reported in this paper.

2. Theoretical Background

2.1. Cumulant Expansion, Line Broadening, and Correlation Functions. A perturbative description of four-wave mixing is well established and described in great detail in the literature;[65,67] we will therefore only discuss elements of this approach that are of direct relevance to this paper. The pulse sequence of the stimulated photon echo (SPE) and the double-sided Feynman diagrams needed in a third-order perturbative description of the photon echo are displayed in Figure 1.

For a two-level system in the rotating-wave approximation the nonlinear polarization generated in the direction $\mathbf{k}_3 + \mathbf{k}_2 - \mathbf{k}_1$ is given by

$$
\begin{aligned}
P^{(3)}(t,t_{12},t_{23}) \propto\ & \\
\exp(-t_{23}/T_1)\int_0^\infty \mathrm{d}t_3\int_0^\infty \mathrm{d}t_2\int_0^\infty \mathrm{d}t_1\{[R_{\mathrm{II}}(t_3,t_2,t_1) + R_{\mathrm{III}}(t_3,t_2,t_1)] \times & \\
E_3(t-t_3)\,E_2(t+t_{12}-t_3-t_2)\,E_1^*(t+t_{12}+t_{23}-t_3-t_2-t_1) \times & \\
\exp[-\mathrm{i}(\omega_{\mathrm{eg}}-\omega)(t_3-t_1)] + [R_{\mathrm{I}}(t_3,t_2,t_1) + R_{\mathrm{IV}}(t_3,t_2,t_1)] \times & \\
E_3(t-t_3)\,E_2(t+t_{23}-t_3-t_2-t_1)\,E_1^*(t+t_{12}+t_{23}-t_3-t_2) \times & \\
\exp[-\mathrm{i}(\omega_{\mathrm{eg}}-\omega)(t_3+t_1)]\} + \exp(-t_{23}/T_1) \times & \\
\int_0^\infty \mathrm{d}t_3\int_0^\infty \mathrm{d}t_2\int_0^\infty \mathrm{d}t_1\{[R_{\mathrm{II}}(t_3,t_2,t_1) + R_{\mathrm{III}}(t_3,t_2,t_1)] \times & \\
E_3(t+t_{12}-t_3-t_2)\,E_2(t-t_3)\,E_1^*(t+t_{12}+t_{23}-t_3-t_2-t_1) \times & \\
\exp[-\mathrm{i}(\omega_{\mathrm{eg}}-\omega)(t_3-t_1)] + [R_{\mathrm{I}}(t_3,t_2,t_1) + R_{\mathrm{IV}}(t_3,t_2,t_1)] \times & \\
E_3(t+t_{23}-t_3-t_2-t_1)\,E_2(t-t_3)\,E_1^*(t+t_{12}+t_{23}-t_3-t_2) \times & \\
\exp[-\mathrm{i}(\omega_{\mathrm{eg}}-\omega)(t_3+t_1)]\} \quad (2) &
\end{aligned}
$$

Here ω_{eg} is the first moment of the absorption spectrum, ω is the frequency of the applied E_1-E_3 fields, t is the time with respect to the third pulse, and T_1 is the population relaxation

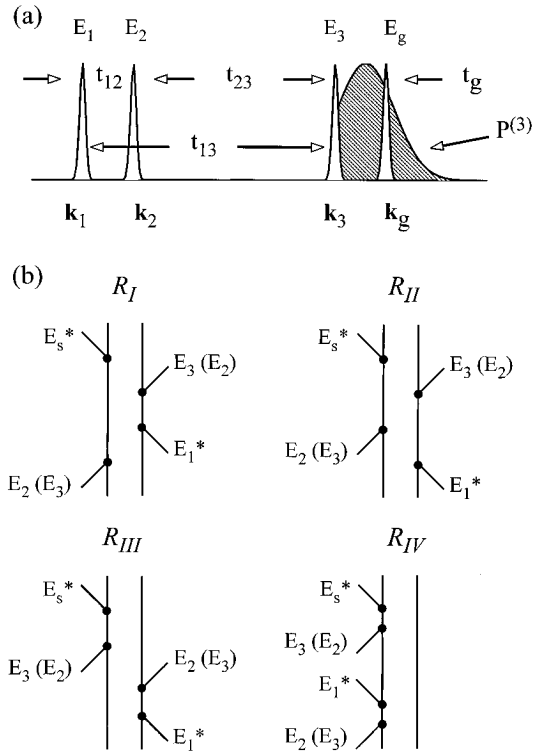

Figure 1. (a) Pulse sequence for the conventional (first three pulses) and time-gated stimulated (all four pulses) photon echo. Relevant delay times t_{12}, t_{13}, t_{23}, t_g are also indicated. (b) Basic Feynman-space diagrams used for a perturbative description of the third-order polarization $P^{(3)}$ with wave vector $\mathbf{k}_3 + \mathbf{k}_2 - \mathbf{k}_1$ in a two-level system with ground state $|g\rangle$ and excited state $|e\rangle$. Rephasing diagrams II and III describe the real echo, while the non-rephasing diagrams II and IV describe the so-called virtual echo signal. The electric fields in parentheses are given for $t_{23} < 0$.

time, which is supposed to be much longer than t_{12} and t. In eq 2 the first triple integral describes the polarization induced by $E_1-E_2-E_3$ ($E_2-E_1-E_3$) pulse sequence, while the second one depicts the $E_1-E_3-E_2$ ($E_3-E_1-E_2$) pulse ordering (Figure 1). The third-order response functions R_I-R_{IV} are derived making use of the cumulant expansion method, which gives:

$$R_I(t_1,t_2,t_3) = \exp[-g^*(t_3)-g(t_1)-g^*(t_2)+g^*(t_2+t_3)+ g(t_1+t_2)-g(t_1+t_2+t_3)] \quad (3a)$$

$$R_{II}(t_1,t_2,t_3) = \exp[-g^*(t_3)-g^*(t_1)+g(t_2)-g(t_2+t_3)- g^*(t_1+t_2)+g^*(t_1+t_2+t_3)] \quad (3b)$$

$$R_{III}(t_1,t_2,t_3) = \exp[-g(t_3)-g^*(t_1)+g^*(t_2)-g^*(t_2+t_3)- g^*(t_1+t_2)+g^*(t_1+t_2+t_3)] \quad (3c)$$

$$R_{IV}(t_1,t_2,t_3) = \exp[-g(t_3)-g(t_1)-g(t_2)+g(t_2+t_3)+g(t_1+t_2)- g(t_1+t_2+t_3)] \quad (3d)$$

The response functions R_{II} and R_{III} describe the conventional photon echo in an inhomogeneously broadened system.[100] The other two response functions (R_I and R_{IV}) describe the so-called virtual echo,[101−103] which always peaks at $t = 0$ regardless of the nature of the line-broadening mechanism.

One of the most important ingredients in the description of time-domain four-wave mixing is the so-called line-broadening function $g(t)$, which is related to the oscillator−bath correlation functions $M'(t)$ and $M''(t)$ in the following way (Chapter 8 of ref 67):

$$g(t) = \Delta^2 \int_0^t d\tau_1 \int_0^{\tau_1} dt_2\, M'(\tau_2) - i\lambda \int_0^t d\tau [1 - M''(\tau)] \quad (4)$$

The correlation functions $M'(t)$ and $M''(t)$ and the static coupling strength parameters Δ and λ are connected to the spectral density $C(\omega)$ as follows:

$$M'(t) = \frac{1}{\Delta^2} \int_0^\infty d\omega\, C(\omega) \coth\frac{\hbar\omega}{2k_B T} \cos \omega t \quad (5a)$$

$$M''(t) = \frac{1}{\lambda} \int_0^\infty d\omega\, \frac{C(\omega)}{\omega} \cos \omega t \quad (5b)$$

$$\Delta^2 = \int_0^\infty d\omega\, C(\omega) \coth\frac{\hbar\omega}{2k_B T} \quad (5c)$$

$$\lambda = \int_0^\infty d\omega \frac{C(\omega)}{\omega} \quad (5d)$$

where k_B is the Boltzmann constant and T is the absolute temperature. The derivation of eqs 2−5 can be found in ref 67.

Equations 5 show that the spectral density $C(\omega)$ is the fundamental quantity in the cumulant expansion formalism and that once $C(\omega)$ is known, all other quantities can be calculated directly. Note that the solvation correlation function as measured, for instance, in a time-gated fluorescence Stokes shift experiment is directly related to $M''(t)$. In contrast, photon echo, as we will show, is primarily sensitive to $M'(t)$, which describes the real part of the line-broadening function $g(t)$.

Given the relation between $M'(t)$ and $M''(t)$ via $C(\omega)$, both functions can be converted one into the other. The spectral density $C(\omega)$ as well as the solvation correlation function $M'(t)$ can be easily derived from $M''(t)$ by use of the following relations:

$$C(\omega) = \lambda \int_0^\infty dt\, M''(t) \cos \omega t \quad (6)$$

$$M'(t) = \frac{\lambda}{\Delta^2} \int_0^\infty d\omega\, \omega \coth(\hbar\omega/2k_B T) \times \cos \omega t \int_0^\infty d\tau\, M''(\tau) \cos \omega\tau \quad (7)$$

In the Brownian oscillator model an exact expression can be calculated for the spectral densities of the individual modes ("generalized solvent coordinates").[67,83] The total spectral density is the sum over all contributions and becomes

$$C(\omega) = \sum_j C_j(\omega) = \frac{2}{\pi} \sum_j \frac{\lambda_j \omega_j^2 \omega \gamma_j}{(\omega_j^2 - \omega^2)^2 + \omega^2 \gamma_j^2} \quad (8)$$

where j numbers the relevant oscillators. Assuming γ_j to be frequency independent, the integration in eqs 5 can readily be performed to obtain analytical expressions for the correlation functions $M'(t)$ and $M''(t)$. Here we restrict ourselves to several simple cases that will be widely used throughout this paper. The more general expression may be found elsewhere.[67,89,90]

First, for a weakly damped mode, $\gamma_j \ll \omega_j$, the correlation functions becomes

$$M(t) \equiv M'(t) \equiv M''(t) = \exp\left(-\frac{\gamma_j t}{2}\right)\left[\cos \omega_j t + \frac{\gamma_j}{2\omega_j} \sin \omega_j t\right] \quad (9)$$

and

$$\lambda = \frac{\Delta^2}{\omega}\tanh\left(\frac{\hbar\omega_j}{2k_BT}\right) \tag{10}$$

If the frequency of the mode is low, $\hbar\omega \ll 2k_BT$, then the high-temperature limit holds and

$$\lambda = \frac{\Delta^2\hbar}{2k_BT} \tag{11}$$

An underdamped mode is usually employed to represent an intramolecular vibration.[83] Another useful example is the case of a strongly overdamped mode, $\gamma_j \gg \omega_j$. In this case, the spectral density can be expressed as follows:

$$C_j(\omega) = \frac{2\lambda_j}{\pi}\frac{\Lambda_j\omega}{\Lambda_j^2 + \omega^2} \tag{12}$$

where $\Lambda_j \equiv \omega^2/\gamma_j$. If in addition the following relation holds, $\hbar\Lambda/(k_BT) \ll 1$, the high-temperature limit applies and the correlation functions $M'(t)$ and $M''(t)$ become indistinguishable:[90]

$$M'(t) = M''(t) = \exp(-\Lambda t) \tag{13}$$

The parameter Λ has a simple physical interpretation: it is the inverse correlation time of the system−bath fluctuations. A strongly overdamped mode is often used to characterize solvation,[83] for instance, in a description of spectral diffusion.

Although the correlation function given by eq 13 is physically appealing, one should be aware of the fact that when for the strongly overdamped mode the high-temperature limit ($\Lambda^{-1} \gg$ 25 fs at room temperature) is not met, the integral in eq 5c diverges. It happens because, after all approximations made, the spectral density in eq 12 decreases as ω^{-1} at high frequencies instead of ω^{-3}, as implied by eq 8. In other words, the short-time behavior of the correlation function given by eq 13 is not correct since the derivative of the correlation function at $t = 0$ is not zero. To overcome this difficulty, one should use eqs 5 and 8 rather than their simplified versions, eqs 12 and 13.

In another approach to this problem one considers a quasi-continuum of undamped ($\gamma_j = 0$) bath modes.[67,84−86] For instance, by choosing a Gaussian distribution of coupling strengths,

$$\lambda_j = \frac{2\lambda}{\sqrt{2\pi}\omega_0}\exp\left(-\frac{\omega_j^2}{2\omega_0^2}\right) \tag{14}$$

we arrive at the expressions for the total spectral density and the correlation function $M''(t)$:

$$C(\omega) = \frac{2\lambda\omega}{\sqrt{2\pi}\omega_0}\exp\left(-\frac{\omega^2}{2\omega_0^2}\right) \tag{15}$$

$$M''(t) = \exp\left(-\frac{\omega_0^2 t^2}{2}\right) \tag{16}$$

Equation 16 is well-known in the theories of solvation dynamics.[70−80] The frequency ω_0 is often called the solvation frequency.

Finally, let us address the physical meaning of the coupling strength parameters Δ and λ. To do so, we consider the expressions for absorption and emission line shapes, which are given by (shifted) Fourier-transformations of the line-shape function $g(t)$:[67]

$$\sigma_{ABS}(\omega) \propto \mathrm{Re}\int_0^\infty \mathrm{d}t\, \exp[\mathrm{i}(\omega-\omega_{eg})t - g(t)] \tag{17}$$

$$\sigma_{EM}(\omega) \propto \mathrm{Re}\int_0^\infty \mathrm{d}t\, \exp[\mathrm{i}(\omega-\omega_{eg}+2\lambda)t - g^*(t)] \tag{18}$$

Therefore, Δ, which is related to the real part of the line-shape function, represents the width of the absorption and/or emission spectra, while 2λ is the Stokes shift, usually associated with the solvation reorganization energy. Note, however, that in deriving eq 18 it is implicitly assumed that relaxation of the excited state toward a new equilibrium position occurs much faster than that of population decay. Otherwise, the Stokes shift becomes dependent on this lifetime and has no simple connection to λ.[104]

The last point to be aware of is the fact that the final system−bath correlation function crucially depends on the choice of system and bath. The separation in system and bath degrees of freedom is a matter of convenience rather than principle.[67] In this paper we have chosen to define our system as a two-level system comprised of the ground and electronically excited state of the dye molecule. The underlying vibrational structure in the optical spectrum of the dye can be taken into consideration by including either the underdamped mode (eq 9) for prominent vibrational modes or the Gaussian mode (eq 16) for a vibrational (quasi)continuum. By such a choice the relevant *intrachromophore* degrees of freedom are projected into the system−bath correlation function. When a correlation function is found that properly describes the optical dynamics, the system could be redefined by projecting the intrachromophore vibrations into a newly defined system, comprised of a vibration-dressed electronic manifold. The new correlation function resulting from such a choice would then only reflect the solute−solvent dynamics. The same procedure can be followed for the dissection of the spectral densities, as is done in section 4.5.

2.2. Time-Integrated Echo-Peak Shift. In an echo-peak shift experiment we measure the maximum of the stimulated photon echo (SPE) intensity for a fixed delay between the second and third excitation pulse (t_{23}) while scanning t_{12}:

$$S_{INT}(t_{23},t_{12}) = \int_0^\infty |P^{(3)}_{SPE}(t,t_{23},t_{12})|^2\, \mathrm{d}t \tag{19}$$

The shift is measured with respect to zero delay between the first two excitation pulses: $t_{12} = 0$.

Recently we demonstrated that under certain conditions a plot of the echo-peak shift as a function of the waiting time t_{23} exhibits a remarkable resemblance to the system−bath correlation function and that this similarity persists even when the finite excitation pulse duration is taken into account.[95] Figure 2 provides a realistic example of this effect in the case of a dye solution. We took the correlation function as depicted in Figure 2a and the calculated echo-peak shift using eqs 2−5 and 19. For the temporal pulse envelope, a sech^2 profile with a fwhm of 14 fs was assumed, while the coupling strength Δ and laser detuning from the transition frequency $\omega_{eg} - \omega$ were set at 265 and 460 cm^{-1}, respectively. Note that the echo-peak shift function depends on whether the delay t_{23} or t_{13} is fixed. This is linked to vibrational dynamics, which manifest themselves as quantum beats in the echo-peak shift (*vide infra*).

Here we shall extend our previous analysis[95] to the situation where the high-temperature limit no longer holds. We begin with some simplifications of eqs 2 and 3. First, we consider the excitation pulses to be infinitely short: $E_i(t) \propto \delta(t)$. More precisely, the inverse bandwidth of the transform-limited pulse must be much broader than both the emission and absorption spectrum of the system. Secondly, the delays between the first and the second as well as the second and the third excitation pulses are taken to be positive: t_{12}, $t_{23} > 0$. Under these assumptions, the SPE intensity can be expressed as follows:[105]

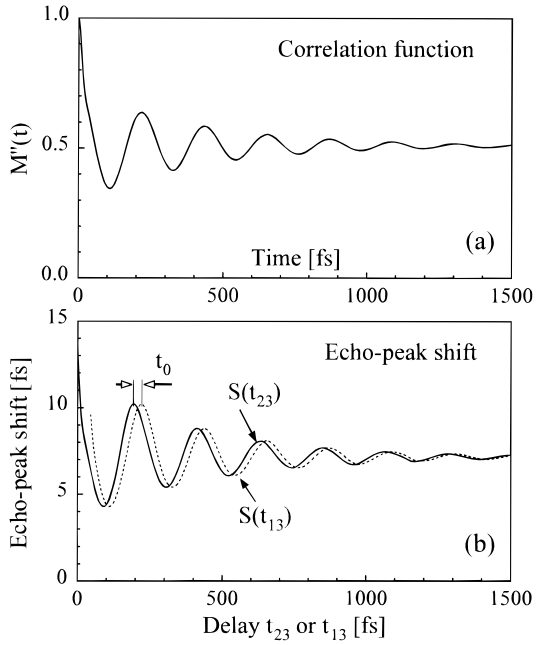

Figure 2. Model correlation function (a) and calculated echo-peak shift function for finite pulse duration excitation (b). Echo-peak shift functions calculated for 14-fs excitation pulses and displayed for t_{23} fixed ($S(t_{23})$) and t_{13} fixed ($S(t_{13})$). Note the remarkable similarity between the correlation function and the echo-peak shift.

$$I_{\mathrm{SPE}}(t,t_{23},t_{12}) = |P^{(3)}(t,t_{23},t_{12})|^2 \propto \exp(-2t_{23}/T_1) \times \cos^2\{\mathrm{Im}[g(t)+g(t_{23})-g(t+t_{23})]\} \times \exp\{-2\mathrm{Re}[g(t)+g(t_{12})-g(t_{23})+g(t+t_{23})+g(t_{12}+t_{23})-g(t+t_{12}+t_{23})]\} \quad (20)$$

As before, we will consider a correlation function that exhibits a fast part followed by a slower tail:

$$M'(t) = (1-a)M'_{\mathrm{fast}}(t) + aM'_{\mathrm{slow}}(t), \quad 0 \le a \le 1 \quad (21)$$

For molecules in liquids such a correlation function is often relevant. The fast part of $M'(t)$ is due to (multiple) wave packet dynamics in combination with the inertial solvation effect. To have the echo-shift function track the correlation function, two assumptions have to be made. First, the fast part of the correlation function must decay to zero by the time t_{23}: $M'_{\mathrm{fast}}(t_{23}) = 0$. Second, the slow part of $M'(t)$ must be stationary on the time scales of t and t_{12}. With these assumptions we can expand $g(t + t_{23})$, etc., in eq 20 in a Taylor series around t_{23}, which results in the following simplified form of the transient echo signal:

$$I_{\mathrm{SPE}}(t,t_{23},t_{12}) = \cos^2\left\{\lambda_{\mathrm{fast}}\int_0^t M''_{\mathrm{fast}}(\tau_1)\mathrm{d}\tau_1 + \lambda_{\mathrm{slow}}t \times [1-M''_{\mathrm{slow}}(t_{23})]\right\} \times \exp\left(-\frac{2t_{23}}{T_1}\right)\exp\left\{-2\Delta^2(1-a) \times \int_0^t \mathrm{d}\tau_1 \int_0^{\tau_2}\mathrm{d}\tau_2 M'_{\mathrm{fast}}(\tau_2) - 2\Delta^2(1-a)\int_0^{t_{12}}\mathrm{d}\tau_1\int_0^{\tau_2}\mathrm{d}\tau_2 M'_{\mathrm{fast}}(\tau_2) - \Delta^2t^2 - \Delta^2t_{12}^2 + 2\Delta^2 t t_{12} aM'_{\mathrm{slow}}(t_{23})\right\} \quad (22)$$

where λ_{slow}, $M''_{\mathrm{slow}}(t)$ and λ_{fast}, $M''_{\mathrm{fast}}(t)$ are related via eqs 5−7 to $a\Delta$, M'_{slow} and $(1-a)\Delta$, M'_{fast}, respectively.

We will now show that as t_{23} is scanned, variations in the cosine term in eq 22 are negligibly small. To do so, we examine the limits of these changes. Using eq 5, it is possible to show that the high-temperature approximation (eq 11) yields the largest value for λ provided that Δ is fixed. Furthermore, we consider the extreme limit that the correlation function $M''_{\mathrm{fast}}(t)$ is constant at the time scale of t. Under these conditions we can recast the $\cos^2$ term in the form

$$\cos^2(...) \approx \cos^2\left\{\frac{\Delta^2\hbar}{2k_{\mathrm{B}}T}t[1-aM''_{\mathrm{slow}}(t_{23})]\right\} \quad (23)$$

At long waiting times t_{23} the correlation function approaches zero ("homogeneously" broadened transition) and the echo peaks at time $t = 0$ ($\cos^2(...) = 1$). At the another extreme, $M'' = 1$, one can estimate $\cos^2(...) \approx 0.7$ by taking typical values of $\Delta \approx 265$ cm^{-1} (50 THz) and $t \approx 20$ fs (*vide infra*) for a dye solution at room temperature. This yields a maximum modulation depth in the $\cos^2$ term of about 30% across the whole range of waiting times t_{23}. As we considered the worst case scenario, in reality the effect of the $\cos^2$ term will be even less and may therefore be disregarded. This also confirms the statement made above that the stimulated photon echo is mainly sensitive to the real part of the line-broadening function $g(t)$. To get access to the imaginary part of $g(t)$ and, thus, $M''(t)$, one should perform a heterodyne-detected echo experiment.[37,67]

Further simplification of eq 22 can be achieved by assuming the correlation function $M'_{\mathrm{fast}}(t)$ not to change appreciably on the time scale t or t_{12}. When this result is substituted into eq 19, we get

$$S_{\mathrm{INT}}(t_{23},t_{12}) \propto \exp\left(-\frac{2t_{23}}{T_1}\right)\exp[-\Delta^2 t_{12}^2(1-a^2M'^2_{\mathrm{slow}})] \times \left\{\frac{\sqrt{\pi}}{2} + \mathrm{erf}[\Delta a M'_{\mathrm{slow}}(t_{23})t_{12}]\right\} \quad (24)$$

where erf(x) is the error function. To obtain the position of the echo-maximum (echo-shift), one has to take the derivative of eq 24 with respect to t_{12} and find the zero-crossing point:

$$aM'_{\mathrm{slow}}(t_{23})\exp[-\Delta^2a^2M'^2_{\mathrm{slow}}(t_{23})\,S(t_{23})^2] - \Delta S(t_{23}) \times [1-a^2M'^2_{\mathrm{slow}}(t_{23})]\left\{\sqrt{\pi} + 2\mathrm{erf}[\Delta aM'_{\mathrm{slow}}(t_{23})\,S(t_{23})]\right\} = 0 \quad (25)$$

where we denoted the echo-peak position as $S(t_{23})$. Finally, assuming the fast part of the correlation function (eq 21) to be dominant and leaving only terms that are linear in a, we get

$$aM'_{\mathrm{slow}}(t_{23}) = \frac{\Delta\sqrt{\pi}S(t_{23})}{1+2\Delta^2S^2(t_{23})} \quad (26)$$

Equation 26 is the main result of this section. It shows that there is a direct link between the slow part of the system−bath correlation function $M'_{\mathrm{slow}}(t)$ and the echo-peak shift $S(t_{23})$ even in the non-high-temperature limit. Using eqs 5−7, the correlation function $M''_{\mathrm{slow}}(t)$ can be readily calculated provided that Δ is known from, for instance, the width of the absorption spectrum. In the high-temperature limit and assuming that $\Delta^2S^2(t_{23}) \ll 1$, we retrieve our previous result:[95]

$$M'_{\mathrm{slow}}(t_{23}) \equiv M''_{\mathrm{slow}}(t_{23}) = \frac{\Delta\sqrt{\pi}}{a}S(t_{23}) \quad (27)$$

Note that the echo-shift tracks the correlation function regardless of population relaxation. It is especially useful when it is not clear whether the time-dependent fluorescence shift is caused by solvation or a wavelength distribution of the fluorescence lifetimes (so-called inhomogeneous relaxation kinetics[106−108]). Furthermore, it can be shown that for *any* correlation function the long time scale dynamics is directly reflected in the echo-peak shift function.

At early times, an inherent discrepancy exists between the correlation function and the echo-peak shift. From first principles it can be demonstrated that the short-time dynamics of the correlation function is inertial; in other words the initial slope of the correlation function must be zero.[70−80] In contrast, the slope of the echo-peak shift is always nonzero. This can be easily demonstrated by expansion of the correlation function near the point $t = 0$ into a Taylor series:

$$M'(t) \simeq 1 - \frac{\omega_0^2 t^2}{2} \tag{28}$$

The slope of the echo shift at zero delay t_{23} is thus calculated to be

$$\left(\frac{\partial S(t_{23})}{\partial t_{23}}\right)_{t_{23}\to+0} = \frac{-1}{2 + \frac{4}{3}\Delta^2 S^2(t_{23}=0)[1 + 2\omega_0^2 S^2(t_{23}=0)]} \tag{29}$$

From eq 29 it follows immediately that the initial slope is negative. Consequently the echo-shift function cannot be employed in a direct way for the elucidation of the short-time dynamics.

The precise point in time from whereon the echo-shift function tracks the correlation function is difficult to locate. It depends in a subtle way on the ratio between the ultrafast and slower part of the correlation function and their time scales. The ultimate test of the deduced correlation function is whether it correctly predicts other spectroscopic observables.

2.3. Echo-Peak Shift and Vibrational Dynamics. In femtosecond optical coherence studies, vibrational or phonon dynamics often play an important role. In particular, in many dyes the optical spectra exhibit strong vibrational structure, which on impulsive excitation leads to wave-packet dynamics.[19−21,91−93,109] It is therefore necessary to examine the effect of wave-packet dynamics on echo-peak shift measurements. To do so, we assume the optical transition to be coupled to a single vibrational mode, which for the case of simplicity is supposed to be undamped ($\gamma_j = 0$). The relevant correlation function can be found in eq 9. After a straightforward calculation we find the following contribution to the stimulated echo intensity, which should be multiplied to eq 19:

$$I_{\text{vibr}} = \exp\left\{2\frac{\Delta^2}{\omega^2}\left[-2 + \cos\omega t + \cos\omega t_{12} + 4\sin\frac{\omega t}{2}\sin\frac{\omega t_{12}}{2}\cos\frac{\omega(t+t_{23}+t_{13})}{2}\right]\right\} \tag{30}$$

Experimentally, when the delay between the first two pulses is scanned, either the delay between pulses 1 and 3 or the delay between pulses 2 and 3 is kept constant (Figure 1). These two cases lead to the following vibrational contributions to the SPE intensity:

$$I_{\text{vibr}} = \exp\left\{2\frac{\Delta^2}{\omega^2}\left[-2 + \cos\omega t + \cos\omega t_{12} + 4\sin\frac{\omega t}{2}\sin\frac{\omega t_{12}}{2}\cos\frac{\omega(2t_{23}+t_{12}+t)}{2}\right]\right\}, \quad t_{23} = \text{const} \tag{31}$$

$$I_{\text{vibr}} = \exp\left\{2\frac{\Delta^2}{\omega^2}\left[-2 + \cos\omega t + \cos\omega t_{12} + 4\sin\frac{\omega t}{2}\sin\frac{\omega t_{12}}{2}\cos\frac{\omega(2t_{13}-t_{12}+t)}{2}\right]\right\}, \quad t_{13} = \text{const}$$

For echo-peak shift experiments, the shift due to solely wave-packet dynamics (we ignore for the moment the other degrees of freedom) is found by taking the derivative of eq 31 with respect to t_{12} and calculating the time τ_m where the derivative is zero and hence the echo has its maximum. We find the following expressions for the echo-peak shift τ_m:

$$\sin\omega\tau_m - 2\sin\frac{\omega t}{2}\cos\frac{\omega(2t_{23}+2\tau_m+t)}{2} = 0, \quad t_{23} = \text{const}$$
$$\sin\omega\tau_m - 2\sin\frac{\omega t}{2}\cos\frac{\omega(2t_{13}-2\tau_m+t)}{2} = 0, \quad t_{13} = \text{const} \tag{32}$$

The first thing to note is that the echo-peak shift is not time-synchronized for the two cases. This fact, not captured in eqs 26 and 27 due to approximations made, should be taken into account when performing echo-peak shift experiments on systems where wave-packet dynamics occurs. It is also important to notice that eqs 32 become identical for $t_{13} = t_{23} + 2\tau_m$. This implies that for a scan where t_{23} is kept constant the echo-peak shift is shifted toward early times compared to the case where t_{13} is kept constant. The two functions therefore exhibit a phase shift with respect to one another, as clearly seen in Figure 2b. It turns out that the echo-peak shift functions for the two cases are virtually identical, except for a time shift that amounts to about 20 fs depending on the duration of the excitation pulses.

2.4. Time-Gated Stimulated Photon Echo. In section 2.2 we have shown that echo-peak shift measurements can effectively be used to obtain a first-order approximation of the *slow* part of the system−bath correlation function $M(t)$. However, two questions still remain unanswered: (i) What is the ratio between the fast and the slow components in $M(t)$ and (ii) how is the characteristic time of the fast component estimated? In this section we shall show how this information can be derived by *time-gating* of the photon echo.

When the photon echo is time-gated, for instance, by mixing the echo signal with a gating pulse in a nonlinear crystal, the following signal is detected by a slow photodetector (Figure 1a):[40,41]

$$S_{\text{gated}}(t_g,t_{23},t_{12}) \propto \int_{-\infty}^{\infty} dt\, |E_{\text{gate}}(t - t_g)|^2 |P^{(3)}_{\text{SPE}}(t,t_{23},t_{12})|^2 \tag{33}$$

In eq 33, E_{gate} represents the electric field profile of the gating pulse. If the gate pulse is short compared to the echo transient $E_{\text{gate}} \propto \delta(t-t_g)$, the signal becomes proportional to the echo profile at time t_g:

$$S_{\text{gated}}(t_g,t_{23},t_{12}) \propto |P^{(3)}_{\text{SPE}}(t_g,t_{23},t_{12})|^2 \tag{34}$$

We proceed now in the following way. First, the maximum of the echo transient (eq 34) is found for any delay between the first two pulses t_{12} at a fixed setting for the waiting time t_{23}. Second, the position of the echo maximum $t_{\max}$ is plotted as a function of t_{12}. Third, the slopes of this plot at different times t_{12} are calculated. These will be shown to contain the desired information on the fast part of $M'(t)$. Again, we assume the same bimodal correlation function as given by eq 21. The maximum of the emitted transient echo signal is found by differentiating eq 22 with respect to t_g and finding the zero crossing. The echo peaks at the position $t_g = t_{\max}$, for which holds

$$(1 - a)\int_0^{t_{\max}} dt\, M'_{\text{fast}}(t) + at_{\max} - aM'_{\text{slow}}(t_{23})t_{12} = 0 \tag{35}$$

From eq 35 follows immediately that the slow part of the

correlation function and the ratio between the fast and slow parts are related to the slopes of the plot of the time-gated echo-maximum function at short and long times t_{12}:

$$\left(\frac{\partial t_{\max}}{\partial t_{12}}\right)_{t_{12}\approx 0} = aM'_{\text{slow}}(t_{23}) \tag{36}$$

$$\left(\frac{\partial t_{\max}}{\partial t_{12}}\right)_{t_{12}\to\infty} = M'_{\text{slow}}(t_{23}) \tag{37}$$

From these calculations one can also define a point in time τ' where a distinct change occurs in the slope of the echo-peak shift function:

$$\tau' = \frac{(1-a)}{a}\frac{\int_0^\infty M'_{\text{fast}}(\tau_1)\,\mathrm{d}t_1}{M'_{\text{slow}}(t_{23})} \tag{38}$$

Since M'_{slow} and a are known from eqs 36 and 37, the break point given by eq 38 may be taken as a measure of the correlation time τ_c of the fast process:

$$\tau_c = \int_0^\infty M'_{\text{fast}}(t)\,\mathrm{d}t \tag{39}$$

It is instructive to compare eqs 36−38 derived for the non-Markovian model with the corresponding ones in the Bloch model:[40,103]

$$\left(\frac{\partial t_{\max}}{\partial t_{12}}\right)_{t_{12}\approx 0} = 0 \tag{40}$$

$$\left(\frac{\partial t_{\max}}{\partial t_{12}}\right)_{t_{12}\to\infty} = 1 \tag{41}$$

$$\tau' = \frac{T'_2{}^2}{T_2} \tag{42}$$

where T'_2 and T_2 are the inhomogeneous and homogeneous phase relaxation times, respectively. The slope for short times (eq 40) is always zero, which reflects the infinitely short correlation time for system−bath interactions in the Bloch model: $M(t) = \delta(t)$. For longer times (eq 41), the slope is always unity, as is expected for truly *static* inhomogeneity $M(t) = 1$. Similar to eq 38, the offset given by eq 42 is directly related to the ratio between inhomogeneous and homogeneous contributions to the optical spectrum.

To illustrate the potential of time-gated stimulated photon echo for probing of the correlation function, we performed calculations on a model system comprised of a fast mode, represented by a Gaussian correlation function (eq 16), and a slow, strongly overdamped mode (eq 13):

$$M''(t) = \frac{1}{2}\exp\left(-\frac{t^2}{t_0{}^2}\right) + \frac{1}{2}\exp(-\Lambda t) \tag{43}$$

with $\tau_0 = 14$ fs and $1/\Lambda = 1$ ps. Figure 3a displays the results of calculations of the echo-maximum position for different waiting times t_{23}, using the exact eq 19. As we expect from our analysis, with increasing waiting time t_{23} the slope of the graph gradually decreases due to phase-memory loss. In accordance with eq 36, a straight-line fit to this echo-maximum function was made for short times ($t_{12} < 20$ fs). For long times ($t_{12} > 70$ fs) a fit to a parabola was found to be superior to a fit to a straight line. The quadratic term accounts for higher order terms in the expansion of $g(t)$, which were disregarded in deriving eq 36. Making use of eqs 36 and 37, we can now deduce $M'_{\text{slow}}(t_{23})$ from the slopes of the fits at different times t_{23} and the ratio a between the fast and the slow parts of $M'(t)$ as well as the correlation time of τ_c via eqs 38 and 39. All the derived parameters were found to fall within ±10% of the input values, which justifies the assumptions made in the derivation of eqs 36−38.

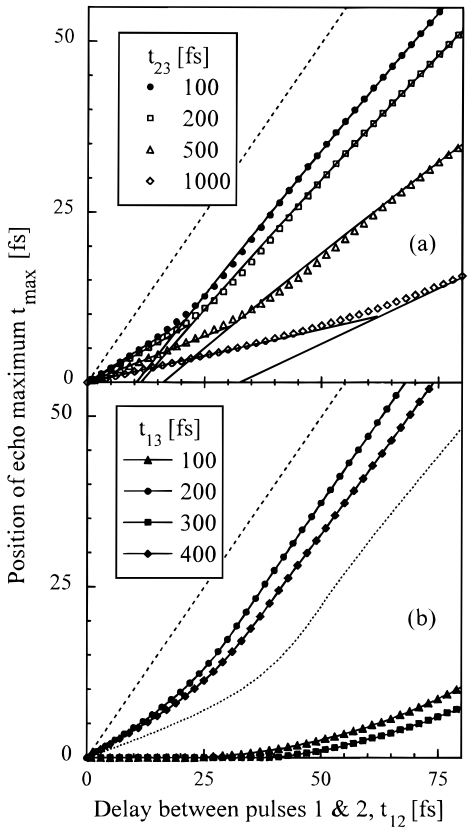

Figure 3. Position of the echo-maximum in time-gated stimulated photon echo as a function of delay t_{12} for two model systems given in eq 43 (a) and eq 44 (b). Panel a displays the effect of different waiting times t_{23} on the slope of the echo-maximum position function. The solid lines in panel a are fits based on eq 36 and eq 37. In panel b the effect of the wave-packet dynamics is shown. The dotted curve refers to the case where the vibrational oscillator is absent with $t_{13} = 100$ fs. The parameters of the oscillators are discussed in the text. The dashed curve in both panels refers to the Bloch model with overwhelming inhomogeneity.

We now turn to a more realistic situation and consider a system that includes also a prominent vibrational mode. To this end an undamped mode is added to the correlation function with the following amplitudes for the different parts:

$$M''(t) = \frac{1}{2}\exp\left(-\frac{t^2}{\tau_0{}^2}\right) + \frac{1}{4}\exp(-\Lambda t) + \frac{1}{4}\cos(\omega_j t) \tag{44}$$

In the simulations we have assumed ω_j to be 330 cm^{-1} and τ_0 and Λ as in eq 43. Figure 3b demonstrates how large the effect can be of a vibrational mode on the time-gated echo. However, when the system is probed at times $t_{13} = 2\pi n/\omega_j$ (n is integer), the curves look similar to those in Figure 3a. It seems that at these times the effect of the vibrational mode is completely suppressed. In contrast, at waiting times $t_{13} = \pi n/\omega_j$ the echo-peak shift curves are severely distorted by the presence of a vibrational mode. For comparison, the dotted line in Figure 3b presents the result in the absence of a vibrational mode.

The dramatic effect of a vibrational mode on the time-gated echo can easily be explained as follows: For $t_{13} = 2\pi n/\omega_j$ the vibrational contribution to the echo signal given by eq 30

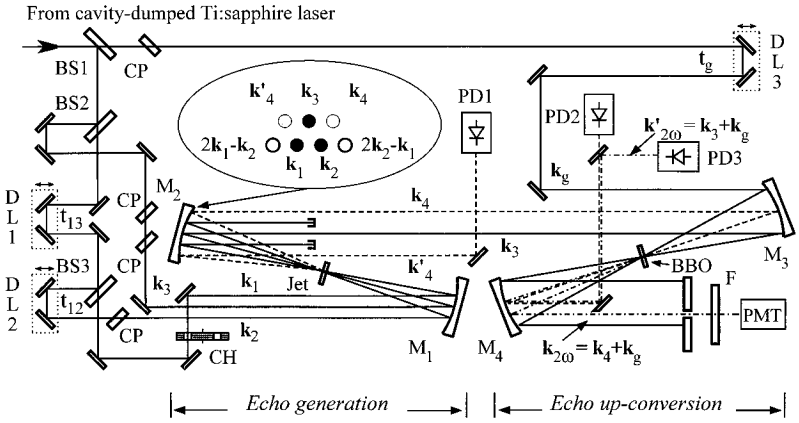

Figure 4. Schematics of the setup to perform conventional and time-gated stimulated photon echo experiments. BS1, BS2, BS3: beamsplitters (T = 70%, 70%, 50%, respectively). CP: antireflection-coated compensation plates. M_1-M_4: r = 25 cm mirrors. Jet: 100-μm jet with sample solution. DL1, DL2, DL3: 0.1-μm precision delay lines. CH: mechanical chopper. PD1−PD3: silicon photodiodes. PMT: photomultiplier tube. BBO: 25-μm or 100-μm β-barium borate crystal for up-conversion. F: filter. The beam geometry near M_2 (inset) depicts the phase-matching geometry used in the experiment. Two-photon echo beams at the conjugated direction are not shown for simplicity.

simplifies to

$$I_{\text{vibr}} \approx \exp\left\{-2\frac{\Delta^2}{\omega_j^2}[1-\cos\omega_j(t-t_{12})]\right\} \qquad (45)$$

At small delay times t, $t_{12} \ll 2\pi/\omega_j$, this expression further reduces to

$$I_{\text{vibr}} \approx \exp[-\Delta^2(t-t_{12})^2] \qquad (46)$$

which corresponds to an inhomogeneous-like contribution to optical dephasing.[109−111] Therefore, a vibrational mode (manifold) generates a certain "inhomogeneous" broadening at $t_{13} = 2\pi/\omega_j$. Thus when the wave packet recurs at $t_{13} = 2\pi n/\omega_j$, the "vibrational inhomogeneity" reaches a maximum, as reflected in Figure 3b. On the other hand, when the wave packet at times $t_{13} = \pi n/\omega_j$ is at its outer turning point, the echo signal due to vibrational dynamics becomes

$$I_{\text{vibr}} \approx \exp[-\Delta^2(t+t_{12})^2] \qquad (47)$$

This contribution to photon echo would have peaked at *negative* times had it not violated causality. The transient echo signal therefore reaches its maximum at zero time, making the system behave as if it were overwhelmingly homogeneously broadened (consult eq 40). This phenomenon is evident in Figure 3b, where for a delay t_{13} of 100 and 300 fs the echo peaks at t = 0 up to a delay $t_{12} \approx 30$ fs.

In our model correlation function (eq 44) an undamped vibrational mode was considered. It is straightforward to include the effect of finite damping. Damping leads to decrease of the slope of the maximum echo position due to reduced ability of the wave packet to refocus even when it recurs. Note that in order to suppress a vibrational mode, t_{13} rather than t_{23} should be fixed.[91−93]

The analysis of Figure 3 allows us to make several recommendations on how to perform a time-gated stimulated echo experiment. First of all, the system's vibrational modes should be well characterized by performing echo-peak shift measurements. Second, the delay of the third pulse should be timed such that the vibrational wave packet has returned to its original position. At this point the vibrational mode just adds inhomogeneity to the system. Third, to characterize the ultrafast part of the correlation function, it is crucial to observe the break point in the plot of echo-maximum position versus delay t_{12}. In practice this break may not be as evident as presented in Figure 3, because of the effect of a finite pulse duration. Nonetheless, if this break point is observed, one may conclude that the system−bath correlation function exhibits a fast component with a correlation time of the same order as spanned by the echo-maximum position in this time domain.

When comparing the above results with those of section 2.2, it is clear that time-gated measurements provide information on both the fast and slow parts of the correlation function. It is thus a more powerful technique than conventional echo-peak shift measurements. On the other hand, the latter echo technique is very attractive due to its simplicity.

3. Experimental Section

The femtosecond excitation pulses used in our experiments were generated by a home-built cavity-dumped Ti:sapphire laser.[112] Actual pulse energies used were in the range 10−15 nJ at a repetition rate of 800 kHz. A four fused silica prism precompressor was set just after the laser to obtain the shortest pulses at the sample position.

The layout of the setup used for the (time-gated) stimulated photon echo experiments is displayed in Figure 4. The three excitation pulses were focused in the sample jet (thickness ≈ 100 μm) using all reflective optics, after having passed the delay lines (DL) for control of t_{12} and t_{23} times. Care was taken to equalize the total amount of dispersive material (introduced by 1-mm fused silica beamsplitters) in each beam path by insertion of compensation plates (CP) at the appropriate places in the setup. From second-harmonic autocorrelation measurements the pulse duration at the point of the sample was found to be about 14 ± 1 fs. The energy of the excitation pulses was kept as low as ∼0.5 nJ to ensure the absence of intensity-dependent effects. For instance, at higher energies the fifth-order processes manifested themselves as a distortion of the integrated echo profiles and even an appearance of a prominent gap around t_{12} = 0.

The phase-matching geometry of the experiment is depicted in the inset of Figure 4. Both the conjugated two-pulse echoes in the directions $2\mathbf{k}_2 - \mathbf{k}_1$ and $2\mathbf{k}_1 - \mathbf{k}_2$ as well as the three-pulse echoes in the directions $\mathbf{k}_4 = \mathbf{k}_3 + \mathbf{k}_2 - \mathbf{k}_1$ and $\mathbf{k}'_4 = \mathbf{k}_3 + \mathbf{k}_1 - \mathbf{k}_2$ were detected simultaneously by silicon photodiodes (PD), processed by lock-in amplifiers, digitized and stored in the computer for further analysis. The exact zero-time between the first and second excitation pulses t_{12} was derived with an accuracy ±1 fs from the symmetry of the two-pulse echo signals. To determine the delay at which $t_{23} = 0$, the point where the shapes of the two- and three-pulse echo signals in $2\mathbf{k}_2 - \mathbf{k}_1$ and $\mathbf{k}_4$ directions became virtually undistinguishable was used.

For more discussion on behavior of echoes around $t_{23} = 0$ we refer to the Appendix.

Two conjugated stimulated echoes are different in a sense that for scanning t_{12} one echo is recorded with a constant delay between pulses 2 and 3 (say, in the $\mathbf{k}_4$ direction), while for the other echo the delay between pulse 1 and 3 is fixed ($\mathbf{k}'_4$ direction). Since these echoes have a different waiting-time dependence, the distance between the two maxima of these echoes cannot be used to deduce the echo-peak shift as far as any vibrational wave-packet dynamics is present (see Figure 2 and discussion in section 2.3). To deal properly with this inherent asymmetry in the experiment, a second series of t_{12} scans are performed, but this time with the delay between pulses 1 and 3 fixed. Effectively, this leads to the reverse situation compared to the first experiment: in the direction where we used to have t_{23}-fixed echo signal ($\mathbf{k}_4$), we now observe the t_{13}-fixed echo signal, and vice versa. These two scans were repeated for every waiting time. Now from the corresponding mirror-imaged echo curves (one from the first and another from the second scan) accurate values of the echo-shifts can be obtained. This method makes the measurements also virtually insensitive to temperature drift in the setup.

For the time-gated experiments, a second fold (*echo up-conversion*) of the setup was used. One of the stimulated photon echo signals was guided to this section to be mixed with the intense (∼5 nJ) gate pulse in a thin (100 or 25 μm) BBO crystal. The resulting second-harmonic signal at the phase-matched direction $\mathbf{k}_{2\omega}$ was detected by a photomultiplier after spectral and spatial filtering of the residual stray light at the fundamental frequency. By avoiding dispersive materials like collimation lenses between the echo generation and echo up-conversion sections, the use of a compressor in the weak echo beam was circumvented.

At the early stages of time-gated photon echo experiments we faced the problem of jet thickness instability at long times, which led to a drift of the time at which the echo signal and the gate pulse arrive at the up-conversion section. Moreover, since the beam paths for excitation and gate pulses are widely separated (Figure 4), any temperature instability influenced their path difference more severely than in the conventional stimulated echo. The overall drift between the echo and the gate pulse was measured to be as much as 20−30 fs (5−10 μm) over several hours, which obviously was unacceptable. We solved this problem in the following way: The third excitation pulse with wave vector $\mathbf{k}_3$, after having passed through the sample jet, was also directed to the echo up-conversion section and cross-correlated with the same gate pulse. By doing so we created an intrinsic time-zero reference from which we could accurately deduce the position of the time-resolved echo profile.

Dye solutions of DTTCI (Lambda Physik) were prepared with three different solvents: ethylene glycol, methanol, and acetonitrile (Merck p.a.), with maximum optical density over the sample jet of about OD = 0.15−0.2. The spectrum of the laser pulses peaked around 780 nm and overlapped appreciably with the absorption spectrum of the dye molecules.

A measurement cycle took typically 20−30 h. To perform experiments over this extended period of time, the femtosecond spectrometer was put under full automated computer control. The idle output beam of the femtosecond cavity-dumped Ti:sapphire laser was constantly monitored by measuring the laser spectrum, as well as the intensity of the second harmonic signal. On the basis of these characteristic values the operation of the cavity-dumped laser was judged and if needed corrected. The measuring program allowed us to perform a large sequence of different scans. It also monitored zero-delay times in a manner described above and compensated for the drifts if necessary.

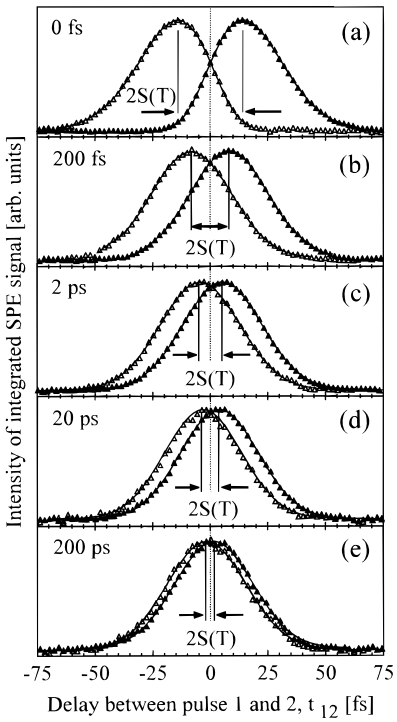

Figure 5. Stimulated photon echo signals for DTTCI in ethylene glycol as a function of the delay t_{12}. Results are given for $\mathbf{k}_4 = \mathbf{k}_3 + \mathbf{k}_2 - \mathbf{k}_1$ (solid triangles) as well as $\mathbf{k}'_4 = \mathbf{k}_3 + \mathbf{k}_1 - \mathbf{k}_2$ (open triangles). The echo-peak shift $S(t)$ is measured as half the distance between the adjacent maxima. The delay between the second and third pulses (as they arrive at the sample) is fixed and given in the upper left corner of each panel. The solid lines are fits to polynomial (a) and Gaussian (b−e) functions.

To keep track of all relevant characteristics of the setup, a log file was permanently updated by the computer. The complete automation of the setup allowed round-the-clock measurements with little human intervention.

4. Results and Discussion

4.1. Conventional Stimulated Echo-Peak Shift Measurements. Figure 5 depicts results of stimulated photon echo measurements on DTTCI in ethylene glycol. Five (out of a few hundred) representative waiting times are given to illustrate the echo-peak shift dynamics. Note, that each panel of Figure 5 is a composition of two subsequent measurements with either t_{13} (open triangles) or t_{23} (solid triangles) waiting times fixed as explained in the Appendix.

The two pulse echo signals (Figure 5a) are visually asymmetric with a peak-shift of ∼14 fs. However, this does not necessarily mean that there is any inhomogeneity in the system. In fact, for finite pulse duration the maximum of the integrated two-pulse echo is always shifted from zero regardless of the nature of the broadening of the transition. This can be understood as follows: If the system is excited with two infinitely short pulses, the echo signal is absent for negative delays t_{12} and appears only for $t_{12} > 0$ (Figure 1b). For these times, it peaks either at $t_{12} = 0$ for a homogeneously broadened or for $t_{12} > 0$ for an inhomogeneously broadened transition. The effect of real pulses can be considered by convolution of the highly asymmetric echo signal with some effective apparatus function. Apparently, the resulting profile will appear shifted from zero in either case.

With increasing waiting time, the shift between the two SPE signals decreases (Figure 5b−e), whereas the width of the curves is basically unchanged. Even for a waiting time of 200 fs (Figure 5b), the echo signals are almost symmetric around their

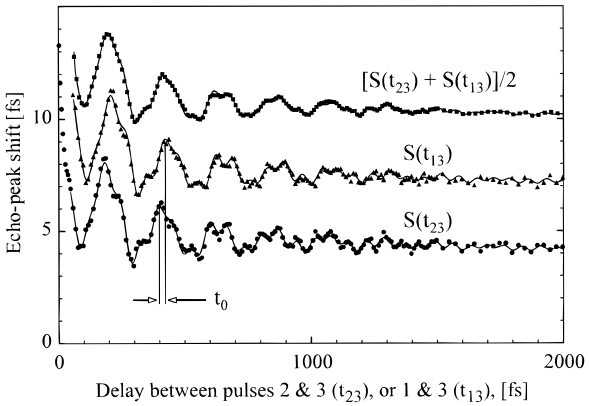

Figure 6. Echo-peak shift functions measured for DTTCI in ethylene glycol. In the lower curve t_{23} is kept constant, $S(t_{23})$, and in the middle curve t_{13} is kept constant, $S(t_{13})$, while the upper one is the average of the lower two. For the sake of clarity, the middle and upper curves are shifted along the vertical axis by 3 and 6 fs, respectively. The solid lines show the fits with two strongly overdamped and three underdamped Brownian oscillators.

maxima and can be fitted fairly well with Gaussian. A simple consideration predicts that the rising flank of the SPE reflects both the inhomogeneous and inhomogeneous contributions, while the falling edge decays with the homogeneous relaxation time.[103] Therefore, the fact that we do not observe any asymmetry in the SPE signal is quite instructive. It gives us the first clue that there must be a substantial relaxation component in the correlation function already faster than 200 fs. At still longer times (∼200 ps) the echo shift becomes close to zero. In physical terms it means that at this time scale the system is overwhelmingly homogeneously broadened and that the photon echo has transformed into a free induction decay.

The recorded data were processed as follows: In each scan the maximum of the time-integrated echo profile was obtained by fitting the data using either a polynomial (t_{23} < 50 fs) or Gaussian function (t_{23} > 50 fs), depending on the asymmetry of the signals. The echo-peak shift was calculated as half the distance between the two corresponding maxima of the fitted profiles. The results of echo-peak shift measurements obtained from combining a few hundred scans are depicted in Figure 6. One of the curves was measured with t_{13} constant, and the other with t_{23} being fixed. Note that it is not possible to define properly the echo-peak shift of t_{13}-scanned profiles for $t_{13} \leq$ 50 fs because of interference between different pulse permutations (see the Appendix).

Here we focus on two points regarding these curves. The first one is that the echo-shift functions for fixed t_{13} or fixed t_{23} look very similar, except for a time-shift of ∼20 fs, indicated by t_0. This observation accords with the analysis presented in section 2.3. The second point concerns the quantum beats observed in both echo-shift functions. These beats are due to wave-packet dynamics in the both ground and excited states.[37,94,95,98] Fourier transformation shows that the active modes have frequencies of 155, 380, and 485 cm^{-1}. The origin of quantum beats in the echo-peak shift was also discussed in section 2.3. Note that when the average of the two is taken (upper curve)—this is effectively done when the shift is calculated from the distance between the echo-maxima where two conjugated echoes are measured simultaneously[96,97]—the modulation at higher frequencies is lost.

Figure 7 displays the results of echo-peak shift measurements on solutions of DTTCI in ethylene glycol, methanol, and acetonitrile. On the basis of the spread in the data, the accuracy in the measured echo-peak shift is estimated to be better than 0.3 fs for ethylene glycol and ∼0.5 fs for methanol and acetonitrile. The solid lines are fits based on a system−bath

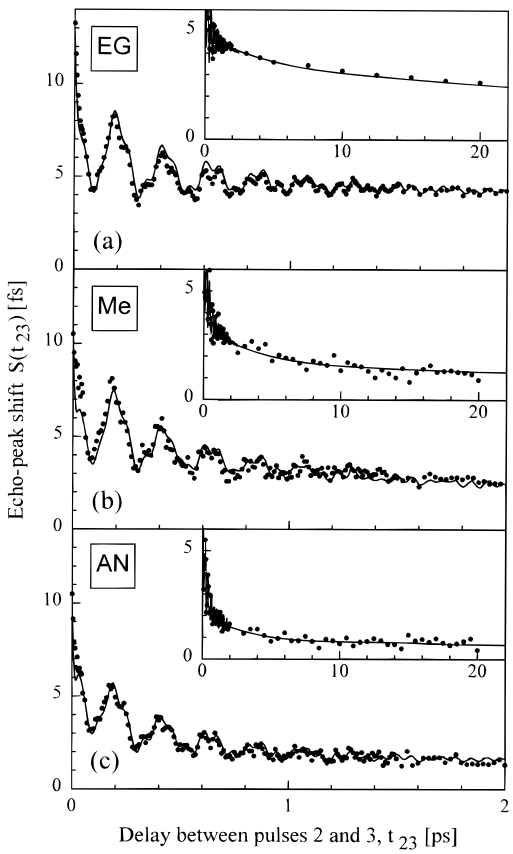

Figure 7. Echo-shift functions obtained for DTTCI in ethylene glycol (a), methanol (b), and acetonitrile (c). The insets show the long time behavior for delays t_{23} up to 20 ps. Solid lines are calculations as described in section 4.3.

correlation function discussed in section 4.3. In all three solvents nearly identical quantum beats are observed, strongly supporting the idea that this beating effect is due to *intrachromophore* vibrational dynamics in the probe molecule. As pointed out earlier, these quantum beats are due to wave-packet dynamics originating from a 155 cm^{-1} mode, although higher frequency beats are clearly present as well. While the intrachromophore vibrational dynamics are similar in all solvents, the solute−solvent dynamics are very different, as evident from the insets. In ethylene glycol the echo-peak shift decays on a time scale of 50−200 ps (not shown), while in methanol and acetonitrile this decay proceeds on time scales of 5 and 3 ps, respectively. These long time dynamics of the correlation function are certainly caused by diffusive solvent motions and generate an overall "inhomogeneity" of the transition. However, this inhomogeneity is not static but dynamical on the aforementioned time scales, leading to spectral diffusion across the optical transition.

The last point to be discussed about Figure 7 is a small (∼0.5−0.7 fs) residual echo-peak shift at very long times, most apparent for acetonitrile (Figure 7c). In the time-window of our measurements (∼0.5 ns) we were not able to observe any appreciable decay of this component. Although it would be conceivable that this residual shift is due to higher order nonlinearities (i.e., $\chi^{(5)}$),[98] this is definitely not the case in our experiments, as we inferred the same long-time peak-shift with the excitation pulses strongly attenuated. Since very small angles between the excitation beams were used, it is also unlikely that this shift is due to the noncollinear geometry of the experiment. Therefore, we believe that the echo-peak shift at these long times is not an artifact but that it shows that even at a nanosecond time scale there is some inhomogeneity left in the system.

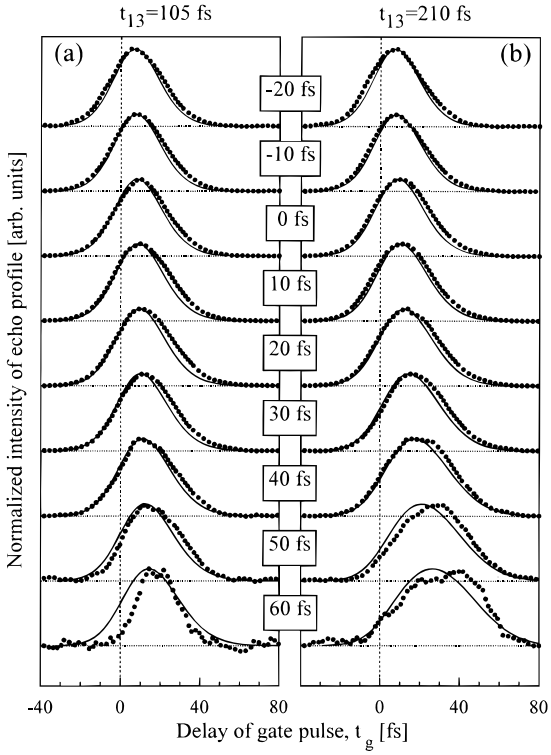

Figure 8. Stimulated photon echo profiles (solid circles) as derived from time-gated experiment, at $t_{13} = 105$ fs (a) and 210 fs (b) for DTTCI in ethylene glycol. Solid lines are fits as described in section 4.3, while dashed lines show the position of the third excitation pulse.

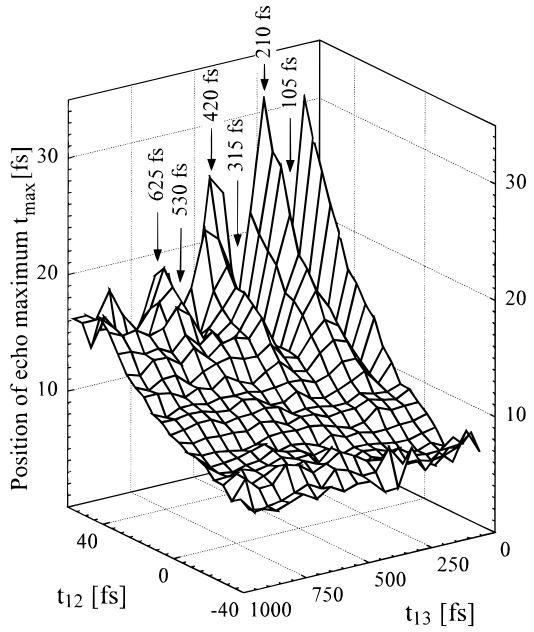

Figure 9. Position of the time-gated echo-maximum as a function of delay t_{12} and waiting time t_{13} for DTTCI in ethylene glycol. The strong modulation due to the 155 cm^{-1} mode is clearly visible. The arrows and numbers indicate the waiting times t_{13} for which maximum and minimum modulation depth is observed. Note that the shift of the echo-maximum is directly correlated with the wave packet's position.

4.2. Time-Gated Stimulated Photon Echo Experiments. Time-gated echo measurements play an extremely important role as a check on the overall correlation function; especially important is the fact that it provides access to the conjectured ultrafast component in it. Figure 8 displays a characteristic set of time-gated echo profiles for DTTCI in ethylene glycol for delay times t_{13} of 105 and 210 fs. These specific delays are taken because at 105 fs the wave packet is at its outer turning point, whereas at 210 fs it has returned from its journey. In the latter case, the effect of the wave packet at short times is analogous to that of inhomogeneous broadening, which reflects itself as an additional shift in time of the echo signal (section 2.4).

At $t_{13} = 105$ fs all echo profiles are asymmetric, with the raising edge steeper than the falling edge. Furthermore, upon changing the delay t_{12} both the position of the signal and its width remain almost unchanged. This agrees well with the predictions of section 2.4 and shows how the wave-packet dynamics of the chromophore make the system behave as overwhelmingly homogeneously broadened. In contrast, for $t_{13} = 210$ fs, an apparent broadening in the time-resolved echo profiles is observed as the separation between the first two pulses increases. The echo profiles become more symmetric and the peak of the echo signal shifts toward longer times. This is a clear signature of the existence of appreciable inhomogeneity in the system. As we discussed in section 2.4, in this case the vibrational mode is suppressed and it "adds" its "vibrational inhomogeneity" (eq 46) to the system.

To find the maximum of the time-gated echo profiles accurately, the transient profiles were fitted by a polynome or Gaussian depending on their asymmetry (not shown in Figure 8). When the time-gated echo-maxima are plotted as a function of delay between the different excitation pulses, Figure 9 is obtained.

Figure 9 shows that the position of echo-maximum exhibits the largest delay at times when the wave packet refocuses. The reason for this behavior is identical to the case of the quantum beat modulations in the echo-peak shift function. At short times and for $t_{13} = 2\pi/\omega$ the wave packet generates dynamics similar to that of inhomogeneous broadening, which leads to a shift in the echo-maximum. When cuts through this figure are made for constant t_{13}, one observes very different dynamics along the t_{12} axis. When at $t_{13} = 210$, 420, and 625 fs the wave packet has refocused, the effect of wave-packet dynamics on the echo decay is suppressed, at least partly. The decay of vibrational dynamics is noticed by the fact that at later refocusing times the echo-maximum position shifts toward shorter times. When the wave packet has reached its outer turning point at $t_{13} =$ 105, 315, and 530 fs, the effect of the wave packet on the echo dynamics is maximal, as is also shown in Figure 3. Note that the quantum beat effect is more pronounced in time-gated echo than in time-integrated echo-peak shift measurements. The effect of time-gating on mode suppression in dye solutions is dealt with in detail in ref 109.

Figure 10 depicts the shifts of echo-maxima at several characteristic delays for DTTCI in ethylene glycol, methanol, and acetonitrile. The dashed curves in Figure 10 are those expected for a system obeying Bloch dynamics, in case the inhomogeneous broadening is overwhelming. Depending on whether the wave packet has refocused, the echo-maximum undergoes a dramatic shift as discussed above. Note that there is a clear break in the echo-peak shift curve at $t_{max} \approx 15$ fs for ethylene glycol at a delay of $t_{13} = 210$ fs (Figure 10a). This supports the notion of dynamics on a 10-fs time scale, as explained in section 2.4. In the other solvents this break point is not so evident, but the simulations are consistent with ultrafast dynamics in these solvents as well. We emphasize that at 205 fs the effect of wave-packet dynamics is negligible, as at this point the wave packet has refocused completely. Also noteworthy in Figure 10 is the change in slope that occurs when the wave packet proceeds from its outer turning points at 110 and 315 fs to its original position at 210 and 420 fs. These variations, seen in all solvents, are explained by the fact that in the latter case the wave packet generates dynamics that look like inhomogeneous broadening, hence the upward bending of

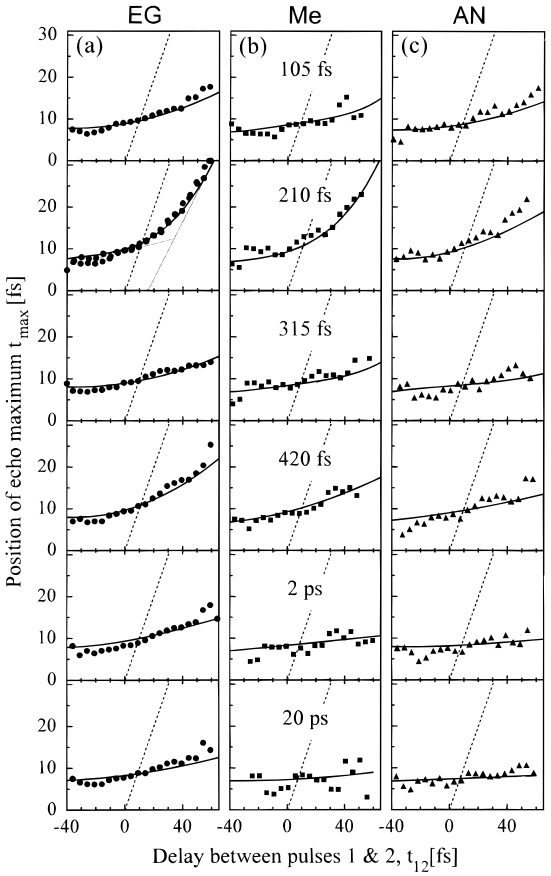

Figure 10. Time-gated echo-maximum position as a function of delay t_{12} for ethylene glycol (a), methanol (b), and acetonitrile (c). The delay between the first excitation pulse and the third pulse t_{13}, indicated in the middle panel (b), also applies for the adjacent panels (a and b). The solid lines are simulations based on the correlation function as discussed in section 4.3. The dotted lines in panel a, $t_{13} = 210$ fs, are fits similar to Figure 3a. The dashed line in each figure is the time-gated echo-shift expected for the Bloch model in the presence of overwhelming inhomogeneity.

the echo-shift curve (see also section 2.4). When the delay t_{13} exceeds the vibrational dephasing time, the slope of the echo-maximum position curves becomes smaller, eventually changing from a slightly bending upward curve to an almost straight horizontal line. At this point the loss of phase memory has transformed the echo into a free induction decay-like signal, which should peak at $t = 0$ for δ-pulse excitation. The offset of ~7 fs is caused by the effect of finite pulse duration. Note also that there is a small residual slope indicating a nonzero inhomogeneity even at long waiting times (Figure 10c, $t_{13} =$ 20 ps). This accords well with our findings in the previous section.

4.3. Numerical Simulations. Figure 11 displays schematically the procedure to get from the echo-peak shift and time-gated echo experiments to a correlation function that, within the framework of the MBO model, provides an optimal description of all linear and nonlinear optical spectroscopies.

The first step is measurement of the echo-peak shift function $S(t_{13})$ or $S(t_{23})$, as described in section 4.1 (Figures 6 and 7). In the latter case one has to be aware of a phase shift compared to the correlation function. Either of these functions (we tested both with identical results) is simulated, starting from 50 fs on, with the minimum number of Brownian oscillators (BOs). Recall that the initial (first 50 fs) part of the echo-peak shift cannot be directly used to represent the correlation function (section 2.2). To fit the echo-peak shift, 6−7 BOs are needed, of which 3 are underdamped (eq 9) and assigned to intrachromophore vibrations; the other 3−4, linked to solute−solvent

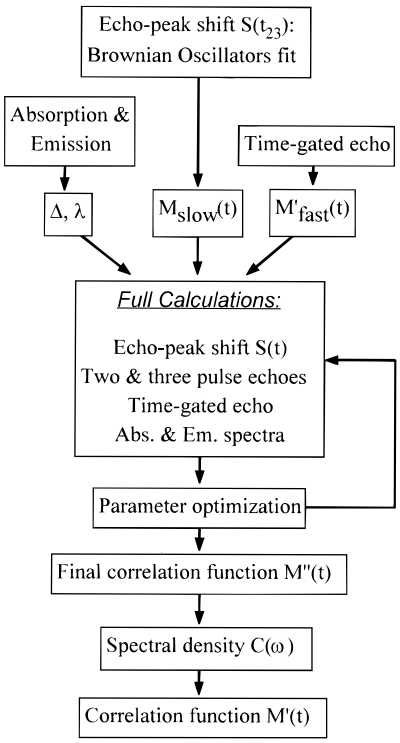

Figure 11. Schematics of the procedure to find the optimal correlation function from conventional and time-gated photon echo and linear optical experiments.

dynamics, are taken as strongly overdamped (eq 13). We also add one Gaussian mode given by eq 16 to represent the part of the correlation function that is believed to appear due to inertial motions of the solvent molecules. The Gaussian profile of this mode follows from the theory[70,78,79] and molecular dynamics simulations.[71−77] Its characteristic time $\tau_0 = \sqrt{2}/\omega_0$ turns out to be approximately 150 fs. On the basis of our experimental data we are unable to conclude whether the Gaussian shape is really of vital importance. For instance, assuming a critically damped ($\omega \approx 2\gamma$, eq 9) or even strongly overdamped (eq 13) BO gives very similar results. However, in the latter case the behavior of the correlation function around zero time is not reflected correctly. One more strongly overdamped BO with $\Lambda^{-1} = 2$ ns is added to represent the residual inhomogeneity evident in Figures 7 and 10. Since this oscillator appears almost static at the time scale of population relaxation (~1 ns), the imaginary part of the line-broadening function $g(t)$ corresponding to this oscillator is not included in the simulations. The resulting fits, shown for the ethylene glycol case in Figure 6, provide a good guess of the relative amplitudes and the correlation times of BOs used as well as the frequencies of the prominent vibrational modes.

The next step is to perform complete simulations with the finite pulse duration explicitly taken into account. From here on, all four nonlinear response functions R_I−R_{IV} (Figure 1b) should be included. The R_I and R_{IV} Liouville pathways cannot be ignored any longer, as they generate a non-negligible contribution to the echo polarization near zero-delay time. Furthermore, all possible pulse permutations (123, 213, 132, 312) and corresponding expressions for the third-order nonlinear polarization (eq 2) are also included in the calculations. Since for finite pulse durations the spectral width of the excitation pulses is reduced, the actual carrier frequency and the shape of the laser pulse become important parameters. In the simulations, the carrier frequency of the excitation pulses is set to 802.5 nm, where the first moment of the laser spectrum lies. A pulse duration of 14 fs is taken, assuming a sech^2 shape for the

TABLE 1: Parameters of the Browning Oscillators Used in Computer Simulations for Ethylene Glycol (EG), Methanol (Me), and Acetonitrile (AN) Solutions of DTTCI (Note That the Actual Weight of the Relevant Mode in the Correlation Function $M''(t)$ Scales as λ)

		EG	Me	AN
solvent modes				
Gaussian mode	λ [cm^{-1}]	17	15	27
	τ_0 [fs]	230	230	140
strongly overdamped modes	λ_1 [cm^{-1}]	20	71	80
	$1/\Lambda_1$ [ps]	0.5	1.0	0.5
	λ_2 [cm^{-1}]	17	26	4
	$1/\Lambda_2$ [ps]	2.5	5	3.3
	λ_3 [cm^{-1}]	51		
	$1/\Lambda_3$ [ps]	50−200		
intramolecular modes				
Gaussian mode	λ [cm^{-1}]		87	
	τ_0 [fs]		14	
underdamped vibrational modes	λ_1 [cm^{-1}]		48	
	ω_1 [cm^{-1}]		150	
	$1/\gamma_1$ [fs]		250	
	λ_2 [cm^{-1}]		3.5	
	ω_2 [cm^{-1}]		380	
	$1/\gamma_2$ [fs]		500	
	λ_3 [cm^{-1}]		11	
	ω_3 [cm^{-1}]		485	
	$1/\gamma_3$ [fs]		670	
inhomogeneous mode	λ [cm^{-1}]		46	
	$1/\Lambda$		>2 ns	

intensity envelope. At this point one more Gaussian ultrafast mode is introduced to comply with the time-gated echo experiments (section 4.2). The necessary input for the coupling strengths Δ and λ was obtained from the simultaneous fit to the optical spectra.

To calculate the transient echo signal, the 3-fold integral given by eq 2 over a combination of the nonlinear response functions, actual pulse shapes, and detuning factors has to be evaluated numerically. After that, the transient is either integrated over time to obtain the stimulated photon echo intensity (eq 19) or convoluted with the gate pulse to compare with the experimental time-resolved echo profiles (eq 33). All calculations, although rather straightforward, are quite time-consuming. For instance, the simulation of a single echo-peak shift curve, as depicted by a solid line in Figure 7, takes about 3 h on a 32-parallel-processors CRAY J932 supercomputer.

With the above set of oscillators and finite excitation pulse width, we can now simulate the echo-peak shift (Figure 7) and time-gated echo (Figure 10) measurements. After comparison between the calculated echo-peak shift curve and the experimental one, the amount of "inhomogeneous" (slowest oscillator) versus "homogeneous" (fastest oscillator) broadening is adjusted to get the zero-delay and the long-time echo-peak shifts right. At the same time, the correlation time of the fastest oscillator is varied to obtain a break point which is evident in the plot of the echo-maximum position. From here on convergence to the optimal correlation function is achieved by fine tuning of the parameters such that the echo-peak shift and time-gated echo as well as the optical spectra were finally reproduced. To perform this convergence procedure effectively, the use of a supercomputer is essential.

The set of the BO parameters that describe the correlation function $M''(t)$ best of all, is presented in Table 1, while the fits to the experimental data are given by solid lines in Figures 7, 8, and 10. Variation of any of the parameters by only ±10% leads to a noticeable degradation of the overall quality of the fit. However, the simultaneous variation of several parameters turns out to be quite tolerable. For instance, the correlation time of the Gaussian solvent mode can be made somewhat longer (shorter) if the correlation time of the next strongly overdamped BO is shortened (elongated) with some minor adjustment in their relative amplitudes. Finally, the spectral density $C(\omega)$ and the correlation function $M'(t)$ are calculated via eqs 6 and 7.

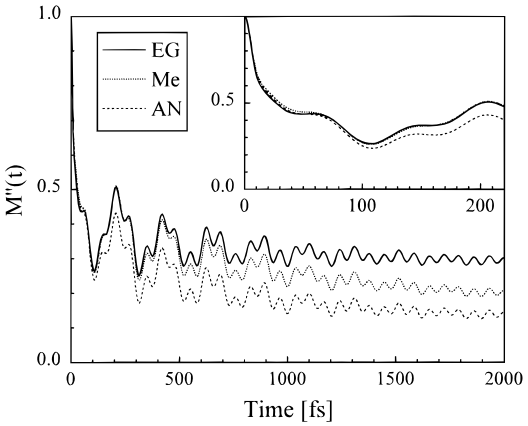

Figure 12. System−bath correlation functions $M''(t)$ for DTTCI in ethylene glycol (solid line), methanol (dotted line), and acetonitrile (dashed line). The inset shows the initial ultrafast part of the correlation functions. The dye molecule is treated as a two-level system interacting with a bath, consisting of both intra- and intermolecular degrees of freedom.

4.4. The Physics behind the Correlation Function. Figure 12 displays the full system−bath correlation functions of the system DTTCI in ethylene glycol, methanol, and acetonitrile. We emphasize that the existence of an ultrafast part in the correlation function was inferred from time-gated photon echo[40] and phase-locked pump−probe[99] experiments. Previous two-pulse photon echo experiments on dye solutions[32] led also to the conclusion that there is an ultrafast component in the correlation function, but at that time it was not clear whether the given interpretation was unique. Regarding Figure 12, also note that the dye's optical transition has been described in terms of an electronic two-level system interacting with a bath comprised of both *intra-* and *intermolecular* degrees of freedom. Consequently all *intrachromophore* vibrational modes that couple to this transition are projected into the correlation function and manifest themselves as quantum beats.[67] The overdamped solvent modes lead to exponentially decaying parts of the correlation function.[67]

Now that the correlation function has been established beyond any doubt the question arises what the physics is behind it. We begin with a discussion of the ultrafast part of $M(t)$ and present two options for its interpretation. The first one is that the fast response is due to inertial solvation dynamics.[10,45,70−80] Molecular dynamics simulation studies[70−80] suggest that on optical excitation an ultrafast solvation step occurs due to random rotational-like motions of individual solvent molecules in the first solvation shell. However, the response time for this effect is on the order of 100−200 fs for the typical solvents[70−80] and not on the 10-fs time scale, with perhaps the exception of water.[113]

The second possibility is that the ultrafast dynamics is due to a free induction-like decay produced by excitation of vibrational structure across the whole absorption band.[22,24,43,110,114−116] While only a few prominent modes are clearly observed as the quantum beats (Figures 6 and 7), there are many vibrational modes that are only weakly coupled to the electronic transition. Vibronic activity of this kind, however, may extend over the whole spectral range of the optical excitation and even beyond, as has been shown in experiments on ultracold polyatomic molecules in supersonic beam expansions[117,118] and in Raman measurements on the dye IR125 (from the same carbocyanine group as DTTCI).[119] Impulsive excitation of this underlying

broad, but almost structureless, vibronic manifold will produce initially a coherence that decays on the time scale of the spectral width excited. We stress that the ultrafast nature of this process is not related to energy relaxation from the initially excited manifold to the surrounding bath. It can be described as a transition from a state with excess nuclear potential energy, but without any nuclear kinetic energy, into a state with reduced potential energy but enhanced nuclear kinetic energy. In nonlinear optical experiments which are sensitive to the potential energy terms, this effect manifests itself as a rapid dephasing-like decay.

In the theory of radiationless processes the aforementioned effect is well-known in the form of a fast component in the fluorescent decay of a gas phase molecule and has been discussed since 1968.[120−126] The initial fast decay becomes faster when the excitation pulse becomes shorter as an increasing number of states are being excited. This initial decay is ascribed to the same effect of dephasing of an initially prepared coherent state that dephases through its time-dependent Hamiltonian. The decay is irreversible and therefore cannot produce a photon echo, as was shown by Yeh and Eberly.[127]

Recent time-gated fluorescence experiments also provide evidence for an ultrafast component in the dynamic Stokes shift, but study of this effect was beyond the capability of this technique.[48,50,128] In the past also correlation-type optical experiments on dye solutions gave a hint for the existence of an ultrafast dynamical effect in the excited state of dye molecules.[115,116] This paper shows that there is no need to resort to an anharmonic mode coupling scheme[81,115,129,130] for an interpretation of this effect. Yet, *classical* MD stimulations do not include instantaneous excitation of the internal vibrational structure of the solute and therefore cannot reveal the ultrafast component due to intrachromophore vibrational dephasing. To do so, one should either employ a fully quantum-mechanical description or combine an analytical description of the electronic transition with subsequent MD stimulations of the system evolution in the ground and excited states.[131]

Following this initial ultrafast decay of $M(t)$, the correlation function decays at a time scale of about 150 fs in all solvents and from 2 to 200 ps depending on solvent. The fastest of these time scales is probably linked to inertial solvation dynamics, a process whereby the first solvation shell reacts to a change of electronic state by uncorrelated free rotation of solvent molecules.[70−72] The time scales we report here are somewhat slower than usually predicted by molecular dynamics simulations.[70−80] We believe that this may also be related to the fact that our probe molecule is much larger than in most simulations. The part of the correlation function decaying on a picosecond time scale is attributed to a diffusion type of solvent motion. Figure 12 shows that this effect is very much solvent dependent, as expected from dielectric solvation theories.[71b] Note that in all solvents there is also a component in the total solute−solvent coupling strength that appears static on the time scale of our experiment (Table 1). The precise nature of this component is presently unclear. In the case of ethylene glycol and methanol, the hydrogen-bonded network may play a role, yet for acetonitrile this is not an option. It is also possible that the "static inhomogeneity" appears due to the presence of two different species (for instance, isomers) of DTTCI with slightly shifted transition frequencies.

The last question we address is whether a multiple time scale correlation function as displayed in Figure 12 characterizes non-Markovian dynamics. First we note that, although the initial dynamics occurs on the time scale of the excitation pulse, it cannot be represented by a δ-function (purely homogeneous broadening), as required by the Bloch model and as often done to describe the nonlinear experiments.[22,33,92,93,96,97] This assumption would generate Lorentzian-shaped absorption and emission line shapes, in clear disagreement with experiments. Moreover, the Bloch model is also inconsistent with the finding of an imaginary component in $g(t)$, as detected in heterodyne-detected phase-locked pump−probe[37,99] and stimulated photon echo.[37,132] A stochastic (Kubo) model is also inadequate for the same reason, although it is more flexible than the Bloch model in modeling dynamics. A final point is that in the Bloch model the inhomogeneity is static, in contrast to what is seen in the correlation function. The conclusion must be that a correlation function as given in Figure 12 does represent truly non-Markovian dynamics. The same statement holds when the system is redefined in terms of a vibration-dressed optical transition interacting with the remaining overdamped solute−solvent modes.

4.5. Spectral Densities Due to Solute−Solvent Dynamics. Once the correlation function $M''(t)$ is known, one can calculate the spectral densities associated with the BOs that comprise the correlation function.[67] As one of the goals in our experiments is the characterization of the solute−solvent dynamics, we have to decide which BOs are intrachromophore and which are due to solute−solvent dynamics. While generally the experiments do not provide the answer to this question, in our case the division into intra- and intermolecular degrees of freedom is quite evident. The underdamped oscillators are certainly due to intrachromophore vibrational dynamics, while other overdamped oscillators can definitely be assigned to solvent dynamics.[95] The ultrafast part in the correlation function was discussed in section 4.4 and also assigned to intrachromophore vibrational dynamics. We are therefore left with only four (three for methanol and acetonitrile) BOs that represent true solute−solvent dynamics.

The solid line in Figure 13 shows the spectral densities calculated according to eq 7 and associated with the oscillators denoted as solvent mode in Table 1. The dotted curves in this figure are the spectral densities as obtained from optical Kerr effect (OKE) measurements.[10−12] The insets show the parts of the correlation function that corresponds to true solvation dynamics. Few remarks are in order before starting a discussion on Figure 13. First, the peak position and the maximum amplitude of the low-frequency modes scale as Λ according to eq 12. Therefore, the modes with $\Lambda^{-1} > 5$ ps lie beyond the frequency window of Figure 13. Second, the OKE data tend to underestimate the low-frequency diffusive modes.[16] Third, even upon the simultaneous variation of the BO parameters, as we discussed in section 4.3, the spectral densities represented in Figure 13 do not undergo any substantial change.

It is clear that solvent motions that generate an anisotropic Raman polarizability are excellent candidates for determining the optical dynamics as well. In fact, the agreement in the case of acetonitrile is remarkable (Figure 13c). The case of acetonitrile is, of course, the most favorable one for comparison: diffusive processes are completed already by ~2 ps (Figure 13c, inset) and hence are easily captured in the OKE experiment. Also acetonitrile is free of complications imposed by the hydrogen-bonding network. Figure 13 also shows that photon echo is not sensitive to some specific molecular motions seen in the OKE. In the case of ethylene glycol these motions (reflecting intermolecular vibrational interactions) are clearly seen as secondary maxima at 115 and 215 cm^{-1} in the OKE spectral density.[11] For methanol the same situation most probably holds. However, if we display the part of the spectral density that is due to the Gaussian mode, avoiding in this way the influence of low-frequency modes (Figure 13, dotted lines), good correspondence with the low-frequency OKE spectral density is found.

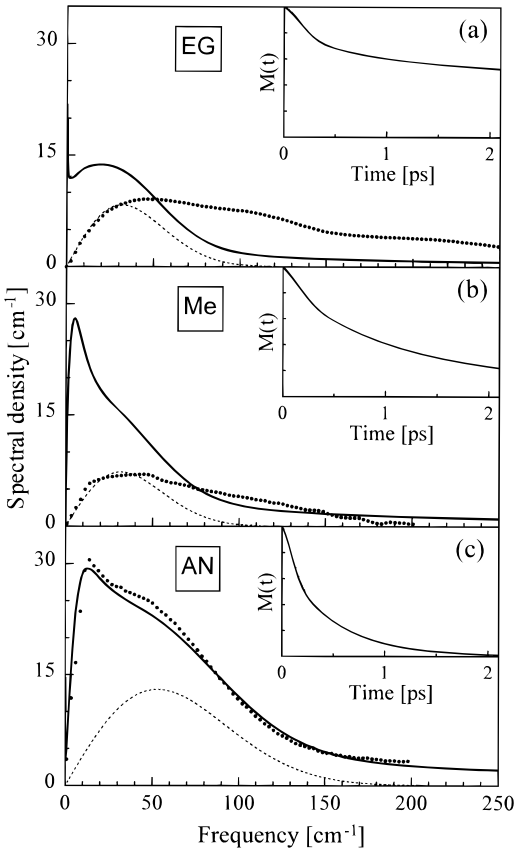

Figure 13. Solute−solvent spectral densities as derived from the correlation function (solid lines) compared to the spectral densities obtained from the optical Kerr effect (solid circles) for ethylene glycol[11] (a), methanol[12] (b), and acetonitrile[10] (c). The experimental data are arbitrarily normalized. The dashed lines show the spectral densities associated with the Gaussian inertial solvent mode. The correlation function ascribed to pure solute−solvent dynamics is presented in the insets.

Several groups have assumed that the OKE probes the same spectral density as that sensed by photon echo.[38,39,41,46] However, whether there is a one-to-one correspondence between what is measured in an OKE and photon echo is very much in doubt, as recently also has been argued.[8,10,14] Moreover, the spectral density covered by the OKE depends on the excitation pulse width used.[9] Currently there is no theoretical justification for assuming that the window on solvent motions provided by the anisotropic Raman polarizability is the same as that presented by photon echo. In particular, we did not see any signature of high-frequency solvent intramolecular modes which were proposed to contribute significantly to the photon echo signals.[39] Despite this lack of a theory, Figure 13 strongly suggests that photon echo senses only the low-frequency part of the spectral density as exposed in the OKE. The nature of this spectral density is not known exactly, but it is probably collision-induced and compares with a phonon sideband in condensed phases.[133] If we adopt here the terminology of the frequency-dependent solute−solvent interactions,[41] the coupling strength between the solvent modes and the chromophore decreases dramatically above ∼150 cm^{-1}. It should also be remarked that photon echo probes *solute−solvent* dynamics and that these dynamics, most likely, are different from *neat-solvent* dynamics.[10] Especially, the molecular dynamics in the first solvation shell will have a solute-specific part.

5. Summary and Epilogue

Figure 14 displays a number of key linear and nonlinear optical experiments on DTTCI in ethylene glycol and simulations based on the deduced correlation function. For methanol and acetonitrile the agreement between experimental results and simulations is also very good. There is no doubt that we have reached our goal of obtaining a correlation function in the MBO framework that fits all data. To the best of our knowledge this is the first time that this has been achieved. This finding also justifies the application of the spin-boson formalism to chemical dynamics in the liquid state. It is also gratifying that only a few Brownian oscillators are needed to simulate the solute−solvent dynamics.

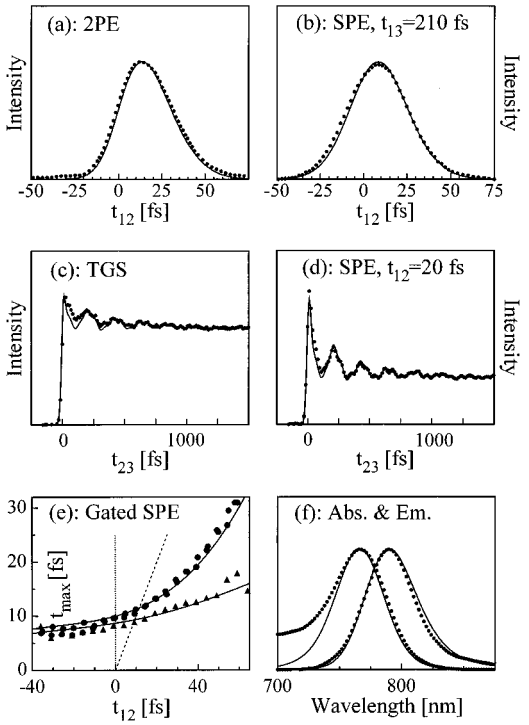

Figure 14. Comparison between results of key linear and nonlinear optical experiments (solid symbols) and simulations (solid lines) based on the deduced system−bath correlation function for DTTCI in ethylene glycol. Two-pulse echo (a), stimulated photon echo at fixed waiting time (b), transient grating scattering (c), stimulated photon echo at fixed delay t_{12} (d), time-gated echo-peak shift for $t_{13} = 210$ fs (circles) and $t_{13} = 2$ ps (triangles) (e), and absorption and emission spectra (f).

The correlation function was acquired by taking as a first-order approximation the echo-peak shift function. From here on numerical calculations were performed including the actual pulse width and compared with the results of several echo and absorption/emission experiments. The use of a supercomputer to reach convergence efficiently was found to be essential.

Now that a recipe has been developed to extract from photon echo experiments a system−bath correlation function that captures the solute−solvent dynamics from femtoseconds to hundreds of picoseconds, the real challenge concerns the interpretation of the underlying physics. For a physical chemist it is essential to try and grasp what can be learned from the system−bath correlation function in relation to chemical reactivity and dynamics in the transition state. This challenge is similar to that faced in magnetic resonance where the electron- or nuclear-spin resonance spectra usually can be fit with great accuracy to a spin Hamiltonian, yet the interpretation of the coupling constants is often not straightforward.[134]

With the arsenal of photon echo techniques described in this paper it is now a rather simple matter to construct a system−bath correlation function in the framework of the MBO model in any material, be it a dye solution, light-harvesting complex, or photosynthetic reaction center.[98] The method may be applicable also to semiconductors, but this has not been attempted yet.

Future work aims at combining photon echo studies with molecular dynamics simulations on molecules smaller than DTTCI. Optical parametric generation techniques now allow for femtosecond pulse generation in the visible part of the spectrum, where smaller molecules absorb. With this approach it is hoped that in the near future a microscopic picture can be obtained of the solute−solvent dynamics and its effect on chemical reactivity.

Acknowledgment. One of us (D.A.W.) dedicates this paper to Robin M. Hochstrasser for showing him how science can be practiced as a form of art. The passionate discussions on spectroscopic problems with Robin and other members of the group left a lasting impression. He also gratefully remembers the good time he and his family had in Philadelphia—*especially the sparkling parties at Robin and Carol's home will never be forgotten*—during his postdoc years, from 1969 to 1971. We are grateful to F. de Haan for providing us with software for efficient data collection and handling and M. F. Emde for help in some of the experiments. We also gratefully acknowledge Dr. E. Riedle and Mrs. G. Kordass from the Max Born Institute (Berlin) for providing us the IR fluorescence spectra of the dye solutions. M.S.P. thanks Prof. V. Shuvalov from the Moscow State University for useful discussions during the Ultrafast Processes in Spectroscopy meeting (Trieste, Italy, Oct 1995). The investigations were supported by the Netherlands Foundation for Chemical Research (SON) and Physical Research (FOM) with financial aid from the Netherlands Organization for the Advancement of Science (NWO).

Note Added in Proof: When the manuscript was under review, a paper entitled "Third-order nonlinear time domain probes of solvation dynamics" by T. Joo, Y. Jia, J.-Y. Yo, M. J. Lang, and G. R. Fleming [*J. Chem. Phys.* **1996**, *104*, 6089] was published. In this study, Joo *et al*. also employed the echo-peak shift as well as the other third-order nonlinear experiments to reveal the system−bath correlation function. Their basic conclusions are qualitatively consistent with those made in the present paper. However, the similarity between the echo-peak shift and the correlation function used by Joo *et al.* was based solely on computer stimulations, and no firm theoretical framework was provided. Furthermore, although time-integrated echo-peak shift measurements give considerable insight in the slow part of the system−bath correlation function, we have shown that use of time-gated SPE proves to be of extreme importance in deducing the ultrafast (intrachromophore) part of the correlation function. In this context it should be mentioned also that one of the strongest vibrational modes in Joo *et al.* study exhibits an unphysically fast (for a Raman-active mode) decay time of 110 fs. This mode may provide the necessary initial ultrafast decay in the correlation function, although its interpretation was entirely different from the one forwarded in this paper. In addition, the deduced inertial part of the solute−solvent correlation function appears to be a factor of 1.5−2 faster than ours.

Appendix. Photon Echo Signals near Zero-Delay Time

In the echo-peak shift experiments, rather complicated behavior of SPE signals is observed whenever the delay between either pulses 1 and 3 or 2 and 3 approaches zero (Figure 15). From consideration of the Feynman diagrams (Figure 1b) follows that SPE signals are generated for any sequence of the three pulses, as long as pulse 1 is not acting as the last one. It gives us four different permutations: 123 (pulse 1 arrives first followed by pulses 2 and 3), 132, 213, and 312. The former two permutations correspond to rephasing (R_{II} *and* R_{III}), while the latter two describe the non-rephasing (R_I *and* R_{IV}) terms.

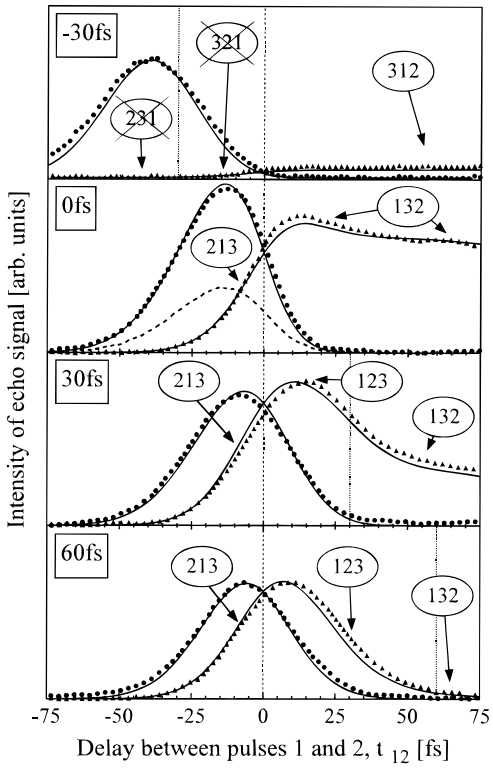

Figure 15. Stimulated echo signals around zero delay t_{13}. Signals are displayed as directly recorded in the experiment in both conjugated directions: $\mathbf{k}_4 = \mathbf{k}_3 + \mathbf{k}_2 - \mathbf{k}_1$ (solid triangles) and $\mathbf{k}'_4 = \mathbf{k}_3 + \mathbf{k}_1 - \mathbf{k}_2$ (open triangles). One of the two pulse echo $\mathbf{k}'_{2PE} = 2\mathbf{k}_1 - \mathbf{k}_2$ is also depicted (dashed line). The pulse sequences that yield the major contributions to the $\mathbf{k}_4 = \mathbf{k}_3 + \mathbf{k}_2 - \mathbf{k}_1$ signal are indicated in the ovals. The dotted line marks the position where the delay between pulses 2 and 3 is equal to zero. The value for t_{13} is given in the upper left corner of each panel. Solid lines are fits with the correlation function as described in section 4.3.

The nonlinear polarizations generated via these contributions should be added up, squared, and integrated in time to obtain the total signal (see eqs 2 and 19). For finite pulse duration, the polarizations overlap in time and therefore interfere. That is why it is not possible to decompose the total echo signal into several components and then convolute them with an effective apparatus resolution function.

In Figure 15, a series of stimulated photon echo signals as they were obtained directly from the experiment are shown. Dashed lines indicate the position in time of the first pulse, and dotted lines represent the third pulse position, while pulse 2 is moved around. In our notations (Figure 1a) this means that for the stimulated photon echo in the direction $\mathbf{k}_4$ (solid triangles), the delay t_{13} is kept constant. The signal in the conjugated $\mathbf{k}'_4$ direction is presented by solid circles.

Let us first consider the stimulated photon echo signal in the direction $\mathbf{k}_4$. For $t_{12} < 0$ (Figure 15a), had the excitation pulses been infinitely short, the signal would have been zero because the 231 and 321 permutations are forbidden in the rotating-wave approximation. However, for the real pulses applied, the nonzero signal is possible due to time overlap of the pulses. For positive t_{12}, the second and the third pulses exchange their position. From this point on, during the delay time t_{12} the system is in the population state that lasts as long as population decay time (∼1 ns). This corresponds to the plateau observed in the experiment.

When $t_{13} = 0$ (Figure 15b), the transient grating spectroscopy configuration is realized. The minor difference is in notations: the grating is written by pulses 1 and 3, while delayed pulse 2 is diffracted. It is well-known that for δ-pulse excitation the

signal is just a step function followed by a long tail with the population relaxation time.[42] Putting it differently, the transient grating spectroscopy, performed with excessively short pulses, yields no information on the dynamics of the system. For our excitation pulses the finite rise time due to pulse overlap ($t_{12} < 0$) is trailed by a plateau with a small modulation due to vibrational coherence.

At positive delays t_{13}, the signal is mainly formed by rephasing contribution. Subsequently, the amplitude of the signal for $t_{13} = 30$ fs (Figure 15c) is higher than negative separation between pulses 1 and 3, $t_{13} = -30$ fs (Figure 15a), when the signal is formed by non-rephasing diagrams. Interference around $t_{12} = t_{13}$ between the pulse sequences that form the peak (123) and the plateau (132) pulls the position of the maximum toward longer delays. Finally, when the t_{13} delay becomes too long for the electron coherence between pulses 1 and 3 to survive, the influence of the 132 contribution becomes negligible. At this point seemingly symmetric (not entirely due to vibrational coherence!) echo signals at two conjugated directions are observed (Figure 15d).

As far as the stimulated photon echo signal at the direction $\mathbf{k}'_4$ is concerned, its behavior can be readily understood if one recalls that the role of pulses 1 and 2 is interchanged due to phase-matching conditions (Figure 4, inset). Hence, what used to be t_{13} delay effectively becomes t_{23} delay now. Subsequently, the echo profile is formed by rephrasing diagrams for *negative* t_{12} and non-rephrasing ones for *positive* t_{12} provided that $t_{13} \geq 0$. Note that for $t_{13} = 0$ the shape of the echo signal is identical to the two pulse echo (Figure 15b, dashed line), which serves as a sensitive probe for finding the zero point in the delay t_{13}.

The discussion above sheds some additional light on the question of whether it is enough to record two echoes at conjugated direction in order to obtain the echo-peak shift function. First, around the delay $t_{13}(t_{23}) = 0$ the position of the maximum of one of the echoes is distorted by the interference between different contributions to the total echo signal. Second, even if these times (t_{13}, t_{23}) are sufficiently long to avoid any interference, the two echo signals still might be nonsymmetric around $t_{12} = 0$ due to vibrational coherence, as discussed in section 2.3. The reason is that for one direction the time between the *first* and the third (in the order they arrive to the sample) pulses is kept constant, while for another (conjugated) direction the constant time is between the *second* and the third pulses. Note that if one performs the scan similar to Figure 15 but with t_{23} fixed, a mirror image of Figure 15 along the $t_{12} = 0$ line is obtained. Now, by combining corresponding signals from two scans, we can compose Figure 5.

References and Notes

(1) Hynes, J. T. *Annu. Rev. Phys. Chem.* **1985**, *36*, 573.
(2) Fleming, G. R.; Wolynes, P. G. *Phys. Today* **1990**, *43*, 36.
(3) Simon, J. D. *Acc. Chem. Res.* **1988**, *21*, 128.
(4) Barbara, P. F.; Jarzeba, W. *Adv. Photochem.* **1990**, *15*, 1.
(5) Rossky, P. J.; Simon, J. D. *Nature* **1994**, *370*, 263.
(6) *Femtosecond Reaction Dynamics*; Wiersma, D. A., Ed.; North Holland: Amsterdam, 1994.
(7) *Femtochemistry: Ultrafast Dynamics of the Chemical Bond*; Zewail, A. H., Ed.; World Scientific: Singapore, 1994.
(8) Lotshaw, W. T.; McMorrow, D.; Thantu, N.; Melinger, J. S.; Kitchenham, R. *J. Raman Spectrosc.* **1995**, *26*, 571.
(9) McMorrow, D.; Lotshaw, W. T. *Chem. Phys. Lett.* **1990**, *174*, 85.
(10) McMorrow, D.; Lotshaw, W. T. *J. Phys. Chem.* **1991**, *95*, 10395.
(11) Chang, Y. J.; Castner, E. W., Jr. *J. Chem. Phys.* **1993**, *99*, 113; *J. Chem. Phys.* **1993**, *99*, 7289.
(12) Cho, M.; Du, M.; Scherer, N. F.; Fleming, G. R. *J. Chem. Phys.* **1993**, *99*, 2410.
(13) Cong, P.; Deuel, H.; Simon, J. D. *Chem. Phys. Lett.* **1993**, *240*, 367.
(14) Duel, H. P.; Cong, P.; Simon, J. D. *J. Phys. Chem.* **1994**, *98*, 12600.
(15) Vöhringer, P.; Scherer, N. F. *J. Phys. Chem.* **1995**, *99*, 2684.
(16) Feldstein, M. J.; Vöhringer, P.; Scherer, N. F. *J. Opt. Soc. Am.* **1995**, *B12*, 1500.
(17) Steffen, T.; Duppen, K. *Phys. Rev. Lett.* **1996**, *76*, 1224.
(18) Cong, P.; Deuel, H.; Simon, J. D. *Chem. Phys. Lett.* **1993**, *212*, 367; *J. Chem. Phys.* **1994**, *100*, 7855.
(19) Fragnito, H. L.; Bigot, J.-Y.; Becker, P. C.; Shank, C. V. *Chem. Phys. Lett.* **1989**, *160*, 101.
(20) Pollard, W. T.; Lee, S.-Y.; Mathies, M. A. *J. Chem. Phys.* **1992**, *7*, 4012.
(21) Bardeen, C. J.; Wang, Q.; Shank, C. V. *Phys. Rev. Lett.* **1995**, *75*, 3410.
(22) Becker, P. C.; Fragnito, H. L.; Bigot, J.-Y.; Brito Cruz, C. H.; Fork, R. L.; Shank, C. V. *Phys. Rev. Lett.* **1989**, *63*, 505.
(23) Pollard, W. T.; Fragnito, H. L.; Bigot, J.-Y.; Shank, C. V.; Mathies, R. A. *Chem. Phys. Lett.* **1990**, *168*, 239.
(24) Bigot, J.-Y.; Portella, M. T.; Schoenlein, R. W.; Bardeen, C. J.; Migus, A.; Shank, C. V. *Phys. Rev. Lett.* **1991**, *66*, 1138.
(25) Nibbering, E. T. J.; Wiersma, D. A.; Duppen, K. *Phys. Rev. Lett.* **1991**, *66*, 2464.
(26) Nibbering, E. T. J.; Wiersma, D. A.; Duppen, K. *J. Photochem. Photobiol.* **1992**, *A62*, 347.
(27) Zhang, R.; Yang, T.-S.; Myers, A. B. *Chem. Phys. Lett.* **1993**, *112*, 541.
(28) Duppen, K.; de Haan, F.; Nibbering, E. T. J.; Wiersma, D. A. *Phys. Rev.* **1993**, *A47*, 5120.
(29) Joo, T.; Albrecht, A. C. *Chem. Phys.* **1993**, *176*, 233.
(30) Nibbering, E. T. J.; Wiersma, D. A.; Duppen, K. *Chem. Phys.* **1994**, *183*, 167.
(31) Duppen, K.; Nibbering, E. T. J.; Wiersma, D. A. In *Femtosecond Reaction Dynamics*; Wiersma, D. A., Ed.; North Holland: Amsterdam, 1994; pp 197−208.
(32) de Boeij, W. P.; Pshenichnikov, M. S.; Duppen, K.; Wiersma, D. A. *Chem. Phys. Lett.* **1994**, *224*, 243.
(33) Bardeen, C. J.; Shank, C. V. *Chem. Phys. Lett.* **1994**, 226, 310.
(34) Rosenthal, S. J.; Schwartz, B. J.; Rossky, P. J. *Chem. Phys. Lett.* **1994**, *229*, 443.
(35) Cho, M.; Fleming, G. R. *J. Chem. Phys.* **1994**, *98*, 3478.
(36) Joo, T.; Jia, Y.; Fleming, G. R. *J. Phys. Chem.* **1995**, *102*, 4063.
(37) de Boeij, W. P.; Pshenichnikov, M. S.; Wiersma, *Chem. Phys. Lett.* **1995**, *238*, 1.
(38) Vöhringer, P.; Arnett, D. C.; Westervelt, R. A.; Feldstein, M. J.; Scherer, N. F. *J. Chem. Phys.* **1995**, *102*, 4027.
(39) Yang, T.-S.; Vöhringer, P.; Arnett, D. C.; Scherer, N. F. *J. Chem. Phys.* **1995**, *103*, 8346.
(40) Pshenichnikov, M. S.; Duppen, K.; Wiersma, D. A. *Phys. Rev. Lett.* **1995**, *74*, 674.
(41) Vöhringer, P.; Arnett, D. C.; Yang, T.-S.; Scherer, N. F. *Chem. Phys. Lett.* **1995**, *237*, 387.
(42) Fainberg, B. D. *Isr. J. Chem.* **1993**, *33*, 225.
(43) Mokhtari, A.; Chesnoy, J.; Laubereau, A. *Chem. Phys. Lett.* **1989**, *155*, 593.
(44) Mokhtari, A.; Chebira, A.; Chesnoy, J. *J. Opt. Soc. Am.* **1990**, *B7*, 1551.
(45) Rosenthal, S. J.; Xie, X.; Du, M.; Fleming, G. R. *J. Chem. Phys.* **1991**, *95*, 4715.
(46) Cho, M.; Rosenthal, S. J.; Scherer, N. F.; Ziegler, L. D.; Fleming, G. R. *J. Chem. Phys.* **1992**, *96*, 5033.
(47) Barbara, P. F.; Walker, G. C.; Smith, T. P. *Science* **1992**, *256*, 975.
(48) Rosenthal, S. J.; Jimenez, R.; Fleming, G. R.; Kumar, P. V.; Maroncelli, M. *J. Mol. Liq.* **1994**, *60*, 25.
(49) Jimenez, R.; Fleming, G. R.; Kumar, P. V.; Maroncelli, M. *Nature* **1994**, *369*, 471.
(50) Horng, M. L.; Gardecki, J.; Papazyan, A.; Maroncelli, M. *J. Phys. Chem.* **1995**, *99*, 17311.
(51) Gustavsson, T.; Baldacchino, G.; Mialocq, J.-C.; Pommeret, S. *Chem. Phys. Lett.* **1995**, *236*, 587.
(52) Vogel, W.; Welsch, D.-G.; Wilhelmi, B. *Phys. Rev.* **1988**, *A37*, 3825.
(53) Vogel, W.; Welsch, D.-G.; Wilhelmi, B. *Chem. Phys. Lett.* **1988**, *153*, 376.
(54) Becker, P. C.; Fork, R. L.; Brito Cruz, C. H.; Gordon, J. P.; Shank, C. V. *Phys. Rev. Lett.* **1988**, *60*, 2462.
(55) Brito Cruz, C. H.; Fork, R. L.; Knox, W. H.; Shank, C. V. *Chem. Phys. Lett.* **1986**, *132*, 341.
(56) Bingemann, D.; Ernsting, N. P. *J. Chem. Phys.* **1995**, *102*, 2691.
(57) Zoidis, E.; Samios, S.; Dorfmüller, Th. *Chem. Phys.* **1992**, *168*, 349.
(58) Zoidis, E.; Besnard, M.; Yarwood, J. *Chem. Phys.* **1995**, *196*, 521.
(59) Madden, P. A. In *Ultrafast Phenomena IV*; Auston, D. A., Eisenthal, K. B., Eds.; Springer: Berlin, 1984; p 244.
(60) Goldberg, S. Y.; Bart, E.; Meltsin, A.; Fainberg, B. D.; Huppert, D. *Chem. Phys.* **1994**, *183*, 217.
(61) Fainberg, B. D. *Phys. Rev. A* **1993**, *48*, 849.
(62) Yajima, T.; Taira, Y. *J. Phys. Soc. Jpn.* **1979**, *47*, 1620.

(63) Grishanin, B. A.; Petnikova, V. M.; Shuvalov, V. V. *Zh. Prikl. Spektrosk.* **1987**, *47*, 966; **1987**, *47*, 1002.
(64) Nibbering, E. T. J.; Wiersma, D. A.; Duppen, K. *J. Chem. Phys.* **1990**, *93*, 5477.
(65) Butcher, P. N.; Cotter, D. *The Elements of Non-Linear Optics*; Cambridge Studies in Modern Optics, Vol. 9; Knight, P. L., Firth, W. J., Eds.; Cambridge University Press: Cambridge, 1995.
(66) Mukamel, S.; Loring, R. F. *J. Opt. Soc. Am.* **1986**, *B3*, 595.
(67) Mukamel, S. *Principles of Nonlinear Optical Spectroscopy*; Oxford University Press New York, 1995.
(68) For experimental verification of the transform relationship between Raman spectoscopies, see: Kinoshita, S.; Kai, Y.; Yamaguchi, M.; Yagi, T. *Phys. Rev. Lett.* **1995**, *75*, 148. Kinoshita, S.; Kai, Y.; Yamaguchi, M.; Yagi, T. *Chem. Phys Lett.* **1995**, *236*, 259. Cong, P.; Simon, J. D.; She, C. Y. *J. Chem. Phys.* **1996**, *104*, 962.
(69) Yan, Y. J.; Fried, L. E.; Mukamel, S. *J. Phys. Chem.* **1989**, *93*, 8149.
(70) van der Zwan, G.; Hynes, J. T. *J. Phys. Chem.* **1985**, *89*, 4181.
(71) Maroncelli, M. *J. Chem. Phys.* **1991**, *94*, 2084; *J. Mol. Liq.* **1993**, *57*, 1. Maroncelli, M.; Fleming, G. R. *J. Chem. Phys.* **1988**, *89*, 5044.
(72) Carter, E. A.; Hynes, J. T. *J. Chem. Phys.* **1991**, *94*, 5961.
(73) Perera, L.; Berkowitz, M. L. *J. Chem. Phys.* **1992**, *96*, 3092; **1992**, *97*, 5253.
(74) Neria, E.; Nitzan, A. *J. Chem. Phys.* **1992**, *96*, 5433.
(75) Maroncelli, M.; Kumar, V. P.; Papazyan, A. *J. Phys. Chem.* **1993**, *97*, 13.
(76) Roy, S.; Komath, S.; Bagchi, B. *J. Chem. Phys.* **1993**, *99*, 3139.
(77) Roy, S.; Bagchi, B. *J. Chem. Phys.* **1993**, *99*, 9938.
(78) Stratt, R. M.; Cho, M. *J. Chem. Phys.* **1994**, *100*, 6700.
(79) Ladanyi, B. M.; Stratt, R. M. *J. Phys. Chem.* **1995**, *99*, 2502.
(80) Kumar, P. V.; Maroncelli, M. *J. Chem. Phys.* **1995**, *103*, 3038.
(81) Aihara, M. *Phys. Rev.* **1982**, *B25*, 53.
(82) Yan, Y. J.; Sparpaglione, M.; Mukamel, S. *J. Phys. Chem.* **1988**, *92*, 4842.
(83) Yan, Y. J.; Mukamel, S. *J. Chem. Phys.* **1988**, *89*, 5160; *Phys. Rev.* **1990**, *A41*, 6485; *J. Chem. Phys.* **1991**, *94*, 179.
(84) Mukamel, S. *Adv. Chem. Phys.* **1988**, *70*, Part I, 165; *Annu. Rev Phys. Chem.* **1990**, *41*, 647.
(85) Caldiera, A. O.; Leggett, A. J. *Physica A* **1983**, *121*, 587.
(86) Grabert, H.; Schramm, P.; Ingold, G. L. *Phys. Rep.* **1988**, *168*, 115.
(87) Cho, M.; Scherer, N. F.; Fleming, G. R.; Mukamel, S. *J. Chem. Phys.* **1992**, *96*, 5618.
(88) Fried, L. E.; Bernstein, N.; Mukamel, S. *Phys. Rev. Lett.* **1992**, *68*, 1842.
(89) Tanimura,Y.; Mukamel, S. *Phys. Rev.* **1993**, *E47*, 118.
(90) Gu, Y.; Widom, A.; Champion, P. M. *J. Chem. Phys.* **1994**, *100*, 2547.
(91) Schoenlein, R. W.; Mittleman, D. M.; Shiang, J. J.; Alivisatos, A. P.; Shank, C. V. *Phys. Rev. Lett.* **1993**, *70*, 1014.
(92) Shank, C. V.; Schoenlein, R. W.; Bardeen, C. J.; Mittleman, D. M. In *Femtosecond Reaction Dynamics*; Wiersma, D. A., Ed.; North Holland: Amsterdam, 1994; pp 125−132.
(93) Bardeen, C. J.; Shank, C. V. *Chem. Phys. Lett.* **1993**, *203*, 535.
(94) Wiersma, D. A.; de Boeij, W. P.; Pshenichnikov, M. S. *Time-resolved femtosecond photon echo as probe of solvent motion*. Invited paper at the Time Resolved Vibrational Spectroscopy-7 Meeting, Santa Fé, NM, June 1995.
(95) de Boeij, W. P.; Pshenichnikov, M. S.; Wiersma, D. A. *Chem. Phys. Lett.* **1996**, *253*, 53.
(96) De Silvestri, S.; Weiner, A. M.; Fujimoto, J. G.; Ippen, E. P. *Chem. Phys. Lett.* **1984**, *112*, 195.
(97) Weiner, A. M.; De Silvestri, S.; Ippen, E. P. *J. Opt. Soc. Am.* **1985**, *B2*, 654.
(98) Joo, T.; Jia, Y.; Yu, J.-Y.; Jonas, D. M.; Fleming, G. R. *J. Phys. Chem.* **1996**, *100*, 2399.
(99) de Boeij, W. P.; Pshenichnikov, M. S.; Wiersma, D. A. *Chem. Phys. Lett.* **1995**, *247*, 264.
(100) Allen, L.; Eberly, J. H. *Optical Resonance and Two-Level Atoms*; Dover, New York, 1975.
(101) Bloom, A. L. *Phys. Rev.* **1955**, *98*, 1105.
(102) Schoemaker, R. L. In *Laser and Coherence Spectroscopy*; Steinfeld, J. I., Ed.; Plenum Press: New York, 1978; p 294.
(103) Duppen, K.; Wiersma, D. A. *J. Opt. Soc. Am.* **1986**, *B3*, 614.
(104) de Boeij, W. P.; Pshenichnikov, M. S.; Wiersma, D. A. Unpublished.
(105) Nibbering, E. T. J. Thesis, University Groningen, 1993.
(106) Agmon, N. *J. Phys. Chem.* **1990**, *94*, 2959.
(107) Fee, R. S.; Milsom, J. A.; Maroncelli, M. *J. Phys. Chem.* **1991**, *95*, 5170.
(108) Blanchard, G. J. *J. Chem. Phys.* **1991**, *95*, 6317.
(109) de Boeij, W. P.; Pshenichnikov, M. S.; Wiersma, D. A. *J. Chem. Phys.*, in press.
(110) Stock, G. *J. Chem. Phys.* **1994**, *101*, 246.
(111) Seidner, L.; Stock, G.; Domcke, W. *J. Chem. Phys.* **1995**, *103*, 3998.
(112) Pshenichnikov, M. S.; de Boeij, W. P.; Wiersma, D. A. *Opt. Lett.* **1994**, *19*, 572.
(113) Fried, L. E.; Bernstein, N.; Mukamel, S. *Phys. Rev. Lett.* **1992**, *68*, 1842.
(114) Lorincz, A.; Novak, F. A.; Rice, S. A. In *Ultrafast Phenomena VI*; Auston, D. H., Eisenthal, K. B., Eds.; Springer Series in Chemical Physics Vol 38; Springer Verlag: Berlin, 1984; p 387.
(115) Taylor, A. J.; Erskine, D. J.; Tang, C. L. *Chem. Phys. Lett.* **1984**, *103*, 430.
(116) Rosker, M. J.; Wise, F. W.; Tang, C. L. *Phys. Rev. Lett.* **1986**, *57*, 321.
(117) Ernsting, N. P.; Asimov, M.; Schäfer, F. P. *Chem. Phys. Lett.* **1982**, *91*, 231.
(118) Hiraya, A.; Shobatake, K. *J. Chem. Phys.* **1991**, *94*, 7700.
(119) Kagan, M. R.; McCreery, R. L. *Anal. Chem.* **1994**, *66*, 4159.
(120) Bixon, M.; Jortner, J. *J. Chem. Phys.* **1968**, *48*, 715. Bixon, M.; Jortner, J. *J. Chem. Phys.* **1969**, *50*, 4061.
(121) Lahmani, F.; Tramer, A.; Tric, C. *J. Chem. Phys.* **1974**, *60*, 4431. Delory, J. M.; Tric, C. *Chem. Phys.* **1974**, *3*, 54.
(122) Jortner, J.; Kommandeur, J. *Chem. Phys.* **1978**, *28*, 273.
(123) Lambert, W. R.; Felker, P. M.; Zewail, A. H. *J. Chem. Phys.* **1981**, *75*, 5958; **1985**, *82*, 297.
(124) Felker, P. M.; Zewail, A. H. *Phys. Rev. Lett.* **1984**, *53*, 501.
(125) Kommandeur, J.; Majewski, W. A.; Meerts, W. L.; Pratt, D. W. *Annu. Rev. Phys. Chem.* **1987**, *38*, 433.
(126) Kommandeur, J. In *Evolution of Size Effect in Chemical Dynamics, Part I*; Prigogine, I., Rice, S. A., Eds.; *Advances in Chemical Physics*, Vol 52; Wiley & Sons: New York, 1988; pp 133−164.
(127) Yeh, J. J.; Eberly, J. H. *Phys. Rev. A* **1980**, *22*, 1124.
(128) Fee, R. S.; Maroncelli, M. *Chem. Phys.* **1994**, *183*, 235.
(129) Fisher, S. F.; Laubereau, A. *Chem. Phys. Lett.* **1975**, *35*, 6.
(130) Diestler, D. J.; Zewail, A. H. *J. Chem. Phys.* **1979**, *71*, 3103
(131) Grishanin, B. A.; Chikishev, A. Yu.; Koroteev, N. I.; Vachev, V.; Zadkov, N. In *Femtosecond Reaction Dynamics*; Wiersma, D. A., Ed.; North Holland: Amsterdam, 1994; pp 169−195.
(132) Pshenichnikov, M. S.; de Boeij, W. P.; Wiersma, D. A. *Phys. Rev. Lett.* **1996**, *76*, 4701.
(133) Di Bartolo, B. *Optical Interactions in Solids*; John Wiley & Sons: New York, 1968.
(134) Carrington, A.; McLachlan, A. D. *Introduction to Magnetic Resonance*; Harper & Row: New York, 1967.

JP961039M